

AD \_\_\_\_\_

Award Number: DAMD17-99-1-9432

TITLE: Dual Modality Imaging System for Breast Cancer Research

PRINCIPAL INVESTIGATOR: Mark B. Williams, Ph.D.

CONTRACTING ORGANIZATION: University of Virginia  
Charlottesville, Virginia 22904

REPORT DATE: July 2004

TYPE OF REPORT: Final

PREPARED FOR: U.S. Army Medical Research and Materiel Command  
Fort Detrick, Maryland 21702-5012

DISTRIBUTION STATEMENT: Approved for Public Release;  
Distribution Unlimited

The views, opinions and/or findings contained in this report are those of the author(s) and should not be construed as an official Department of the Army position, policy or decision unless so designated by other documentation.

20050121 003

**REPORT DOCUMENTATION PAGE**Form Approved  
OMB No. 074-0188

Public reporting burden for this collection of information is estimated to average 1 hour per response, including the time for reviewing instructions, searching existing data sources, gathering and maintaining the data needed, and completing and reviewing this collection of information. Send comments regarding this burden estimate or any other aspect of this collection of information, including suggestions for reducing this burden to Washington Headquarters Services, Directorate for Information Operations and Reports, 1215 Jefferson Davis Highway, Suite 1204, Arlington, VA 22202-4302, and to the Office of Management and Budget, Paperwork Reduction Project (0704-0188), Washington, DC 20503

<b>1. AGENCY USE ONLY</b> (Leave blank)		<b>2. REPORT DATE</b> July 2004	<b>3. REPORT TYPE AND DATES COVERED</b> Final (1 July 1999 - 30 June 2004)	
<b>4. TITLE AND SUBTITLE</b> Dual Modality Imaging System for Breast Cancer Research			<b>5. FUNDING NUMBERS</b> DAMD17-99-1-9432	
<b>6. AUTHOR(S)</b>  Mark B. Williams, Ph.D				
<b>7. PERFORMING ORGANIZATION NAME(S) AND ADDRESS(ES)</b> University of Virginia Charlottesville, Virginia 22904  E-Mail: mbwilliams@virginia.edu			<b>8. PERFORMING ORGANIZATION REPORT NUMBER</b>	
<b>9. SPONSORING / MONITORING AGENCY NAME(S) AND ADDRESS(ES)</b> U.S. Army Medical Research and Materiel Command Fort Detrick, Maryland 21702-5012			<b>10. SPONSORING / MONITORING AGENCY REPORT NUMBER</b>	
<b>11. SUPPLEMENTARY NOTES</b>				
<b>12a. DISTRIBUTION / AVAILABILITY STATEMENT</b> Approved for Public Release; Distribution Unlimited			<b>12b. DISTRIBUTION CODE</b>	
<b>13. Abstract (Maximum 200 Words) (abstract should contain no proprietary or confidential information)</b>  In the 25-40% of the general female population with radiodense breast parenchyma, clinically occult lesions may be invisible in the screen-film mammogram. Even if suspicious masses are detected, determination of the benign or malignant nature of a mass is often impossible from the x-ray image. There is thus a need for diagnostic procedures that can noninvasively help characterize suspicious breast lesions. Scintimammography is an imaging technique that shows promise as an adjunct diagnostic tool in problem solving mammography, for monitoring recurrence after surgery, and in the assessment of multidrug-resistance. However, because clinical Anger cameras have only moderate spatial resolution and are difficult to position close to the breast, small lesions are difficult to detect. In addition, no direct means exists of correlating mammographic and scintigraphic information because of the significantly different shape of the breast in mammography (compressed) and scintimammography (prone, pendulant). We are developing an imaging system that overcomes these problems by combining digital x-ray mammography and gamma emission scintigraphy in a single, integrated system. The system is mounted on a standard upright mammography unit, and can easily be placed in a typical mammography room, providing accessibility even for small breast imaging clinics not associated with major medical centers.				
<b>14. SUBJECT TERMS</b>  breast cancer, scintimammography, digital mammography, dual modality			<b>15. NUMBER OF PAGES</b> 30	
			<b>16. PRICE CODE</b>	
<b>17. SECURITY CLASSIFICATION OF REPORT</b> Unclassified	<b>18. SECURITY CLASSIFICATION OF THIS PAGE</b> Unclassified	<b>19. SECURITY CLASSIFICATION OF ABSTRACT</b> Unclassified	<b>20. LIMITATION OF ABSTRACT</b> Unlimited	

NSN 7540-01-280-5500

Standard Form 298 (Rev. 2-89)  
Prescribed by ANSI Std. Z39-18  
298-102

## Table of Contents

Cover.....	1
SF 298.....	2
Table of Contents .....	3
Introduction .....	4
Body.....	4-7
Key Research Accomplishments.....	7
Reportable Outcomes.....	8,9
Conclusions.....	10
Appendices.....	11

## INTRODUCTION

The purpose of the work funded by this grant is to develop a new type of dedicated system for diagnostic breast imaging that can simultaneously obtain structural information from a digital mammography detector and functional information from a high resolution gamma imaging detector.

The overall goals of the project, as stated in the original application, are:

- a) To upgrade and optimize our test dual system,
- b) To compare its performance over a broad range of phantom imaging tasks to that of the combination of film-screen mammography and scintimammography, and
- c) To perform a limited clinical study in which the results of the dual modality study are compared to the results of biopsy.

## BODY

As taken from the original Statement of Work, the tasks scheduled to begin and/or be completed during the project period are as follows:

*Task 1.* Upgrade digital mammography and gamma detector components of test system, Months 1-6

- a) Replace current 6 cm x 6 cm spot detector with 20 cm x 30 cm full field digital mammography (FFDM) detector
- b) Characterize imaging properties of FFDM detector, including linearity, dynamic range, modulation transfer function (MTF), noise power spectrum (NPS), noise equivalent quanta (NEQ), detective quantum efficiency (DQE), geometric linearity, and artifacts.
- c) Replace 6 cm x 6 cm, 1.25 mm pixel detector with 8 cm x 8 cm, 2.25 pixel detector
- d) Characterize detector imaging properties including sensitivity, line spread function (LSF), energy resolution, geometric linearity, and uniformity of response.
- e) Modify co-registration software to accommodate new detector parameters

*Task 2.* Collimator optimization, Months 3-6

- a) Calculate collimator efficiency, resolution for the range of object distances relevant in the dual system for several potential materials (e.g. tantalum, lead or tungsten).
- b) Fabricate and evaluate small test collimators covering a limited fraction of the FOV, including slant hole collimator.
- c) Build optimized high resolution and optimized high efficiency collimators for dual system.

*Task 3.* Phantom development, Months 7-12

- a) Calculate useful range of phantom parameters (thickness, lesion sizes, etc) based on x-ray and gamma ray attenuation, detector resolution, and scatter measurements.
- b) Fabricate fillable contrast-detail phantoms, chamber phantoms with removable simulated lesions, fillable vessels of various thicknesses to provide background radioactivity, etc.
- c) Purchase breast equivalent mammography block phantoms with imbedded simulated lesions (CIRS, Newport News, VA)
- d) Evaluate dual system performance using permutations of stacked phantoms, scatter free conditions

- e) Repeat the measurements of d), but incorporating the anthropomorphic torso phantom to create realistic scatter conditions.

*Task 4. Quantification of the effects of compression, Months 7-18*

- a) Use the phantoms developed in Task 3 to measure SNR, target-to-background ratio while varying the thickness of interposed phantom material and total phantom thickness

*Task 5. Comparison of dual system performance with diagnostic mammography and scintimammography, Months 19-30*

- a) Repeat the measurements of Tasks 3d-e using a high resolution clinical Anger camera with 10" field of view (Technicare), and clinical screen-film mammography systems (Lorad M-IV, Siemens Mammomat).
- b) Quantify lesion contrast in gamma and x-ray images (using a film densitometer), for both dual and clinical systems.
- c) Perform reader study of contrast-detail images from dual system and from clinical systems. Readers will be physicists, technologists, and radiologists at UVa. Digital x-ray images will be printed to laser film for the study.

*Task 6. Evaluation of multiple gamma and x-ray views, Months 24-30*

- a) Modify phantoms by including blocks (modules) that are composed of heterogeneous materials at several layers to simulate superimposed breast structure
- b) Modify breast support and compression paddle to be fixed and independent of the detector gantry
- c) Use multiple views, single phantom orientation. For each view, obtain corresponding x-ray and gamma ray images.
- d) Evaluate the efficacy of 3-d localization and removal of superimposed structures via tomosynthesis, 3-d reconstruction.

*Task 7. Patient study on dual modality system, Months 24-36*

- a) Update IRB to reflect protocol found most advantageous (i.e. number of views per compression) for lesion conspicuity
- b) Measure uncompressed (pendulant) breast thickness, compressed thickness, and compressive force for each study
- c) Conduct reader study of dual images with two board-certified radiologists (UVa). Correlate reading results with pathology report.

*Task 8. Publication of results, Months 34-36*

## Accomplishments

As detailed in our first year annual report, Task 1 was completed and resulted in a publication in Medical Physics (Williams et al. 1999). The results of Task 2 have also been published, as part of a publication in IEEE Transactions on Nuclear Science (Majewski et al, 2001). Task 3, the development of phantoms, was also essential for the results published in the latter manuscript, as were studies done under Task 4 investigating the effect of breast compression on lesion detectability using phantoms. As described in our report of July 31, 2002, we have completed analysis of the dependence on compressed breast thickness on the scatter to primary ratio, using data obtained in our clinical study (Task 7). These results were presented at the 2002 IEEE Nuclear Science Symposium and Medical Imaging Conference in Newport News, VA, Nov. 10-16, 2002, and have been published in the IEEE Transactions on Nuclear Science (Williams et al., 2003). The results show the measured scatter fraction (fraction of total counts in a given region of interest that are due to scattered gamma rays) as a function of compressed thickness. The data show that compression is likely to reduce the amount of detected scatter.

As we described in our July 31, 2002 report, we have decided that Task 5, as originally proposed, will not be undertaken because in the years since that task was proposed, it has become more clear that it was inappropriately suggested since the scanner is being used in lesion characterization as opposed to lesion detection. Lesion characterization requires accurate assessment of the relative radioactivity concentration in the lesion and surrounding healthy tissue. Quantitation of lesion radiotracer uptake requires corrections for the effects of camera spatial resolution, gamma ray attenuation, and scatter. The first two of these phenomena are functions of the lesion-to-collimator separation, and thus correction requires knowledge of the lesion depth. Therefore, we have invested effort in a) multiple view imaging (originally scheduled as Task 6), and b) development of quantitation tools.

In regard to task a), we described in our July 2002 report the hardware modifications that have been made to a second upright mammography unit to permit multiple images of the breast to be obtained with fixed breast compression. This setup permits highly reproducible, computer controlled positioning of the x-ray tube and a small field of view (5 cm x 5 cm) digital x-ray detector. We have also mounted a larger x-ray detector (20 cm x 30 cm field of view), on the motorized gantry arm. An abstract describing early results of multiple-view, dual modality imaging using phantoms has been accepted for presentation at the IEEE Nuclear Science Symposium and Medical Imaging Conference, October 16-22, 2004, Rome, Italy.

Regarding task b) we have developed a mathematical model whose purpose is to calculate changes in lesion image contrast as a function of the location within the breast of the lesion, breast thickness, and gamma camera position. The results of this work have been presented at several international meetings (the First International Symposium for Functional Breast Imaging in Rome, Italy Rome, Italy, April 18-21, 2001., the IEEE Nuclear Science Symposium and Medical Imaging Conference, Norfolk, VA, November 12-16, 2002, and the 7<sup>th</sup> International Workshop on Digital Mammography, June 18-21, 2004, Durham, NC.), and has led to three publications (see below).

We are completing the reader study associated with our clinical trial. Altogether we have imaged 26 volunteers.

## **Summary**

To summarize, we have now completed all of the Tasks originally proposed except Task 5, which we have learned is inappropriate, and part c) of Task 7, the reader study. We have nearly finished

the reader study, with one reader remaining. This project has resulted thus far in nine publications and eleven scientific presentations. The completion of the reader study will result in at least one more of each. Some of the recent articles are included in the Appendix.

### **KEY RESEARCH ACCOMPLISHMENTS**

- Upgraded dual modality x-ray and gamma ray detectors, with measured performance meeting design specifications, and upgraded the dual modality software
- Optimized gamma camera collimator
- Developed new types of phantoms for evaluation of factors determining lesion contrast in breast scintigraphy
- Quantified the effects of breast compression on lesion contrast in breast scintigraphy
- We have conducted studies leading to the use of an improved gamma camera scintillator material permitting better scatter rejection
- We have evaluated the effects of breast compression on lesion contrast in breast scintigraphy
- We have developed a mathematical model that relates gamma camera resolution and lesion size and depth to image contrast
- We have begun modifications of a second mammography gantry to permit multiple views of the breast with both imaging modalities
- We have investigated methods for scatter correction in the scintimammography images, and have characterized the relationships between the amount of scatter and the location within the breast and overall breast thickness.
- We have obtained very promising preliminary results in our clinical evaluation of the dual modality scanner, and are now completing a reader study to assess the added value of using dual modality scanning to aid in diagnostic workup.

## REPORTABLE OUTCOMES

### Publications

1. Williams MB, More MJ, Narayanan D, Majewski S, Welch B, Wojcik R, and Kieper DA. Phantom Study of Radiotracer Concentration Quantification in Breast Scintigraphy. IEEE Transactions on Nuclear Science June 2003; 50(3):433-438.
2. More MJ, Narayanan D, Goodale PJ, Majewski S, Welch B, Wojcik R, Kieper DA, and Williams MB. X-ray Stereotactic Lesion Localization in Conjunction with Dedicated Scintimammography. IEEE Transactions on Nuclear Science October 2003; 50(5):1636-1642.
3. Williams MB, Narayanan D, More MJ, Goodale PJ, Majewski S, Kieper DA. Analysis of Position-Dependent Compton Scatter in Scintimammography with Mild Compression. IEEE Transactions on Nuclear Science October 2003; 50(5):1643-1649.
4. Williams MB, More MJ, Narayanan D, Majewski S, Weisenberger AG, Wojcik R, Stanton M, Phillips W, and Stewart A. Combined Structural and Functional Imaging of the Breast. Technology in Cancer Research and Treatment 2002; 1:39-42.
5. More MJ, Narayanan D, Goodale PJ, Majewski S, Welch B, Wojcik R, Kieper DA, and Williams MB. X-ray Stereotactic Lesion Localization in Conjunction with Dedicated Scintimammography. IEEE Nuclear Science Symposium and Medical Imaging Conference Record 2002.
6. Williams MB, Narayanan D, More MJ, Goodale PJ, Majewski S, and Kieper DA. Analysis of Position-Dependent Compton Scatter in Scintimammography with Mild Compression. IEEE Nuclear Science Symposium and Medical Imaging Conference Record 2002.
7. Williams MB, More MJ, Narayanan D, Majewski S, Welch B, and Kieper DA. Improved Breast Scintigraphy Using Digital Mammography. IEEE Nuclear Science Symposium and Medical Imaging Conference Record 2001.
8. Majewski S, Kieper D, Curran E, Keppel C, Kross B, Palumbo A, Popov V, Weisenberger AG, Welch B, Wojcik R, Williams MB, Goode AR, More M, and Zhang G. Optimization of Dedicated Scintimammography Procedure Using Detector Prototypes and Compressible Phantoms. IEEE Transactions on Nuclear Science 2001; 48(3):822-829.
9. Williams MB, Goode AR, Galbis-Reig V, Majewski S, Weisenberger AG, and Wojcik R. Performance of a PSPMT Based Detector for Scintimammography. Phys. Medical Biology 2000; 45(3):781-800.



### Scientific Presentations

1. MJ More, PJ Goodale, H Li, Y Zheng, S Majewski, V Popov, B Welch and MB Williams. Limited Angle Dual Modality Breast Imaging. IEEE Nuclear Science Symposium and Medical Imaging Conference, October 16-22, 2004, Rome, Italy.
2. MJ More, PJ Goodale, S Majewski and MB Williams. Evaluation of Gamma Cameras for use in Dedicated Breast Imaging. IEEE Nuclear Science Symposium and Medical Imaging Conference, October 16-22, 2004, Rome, Italy.
3. MJ Moré, PJ Goodale, H Li, Y Zheng and MB Williams. Estimation of Lesion Radiotracer Uptake in Breast Scintigraphy Using Digital Mammography. 7<sup>th</sup> International Workshop on Digital Mammography, June 18-21, 2004, Durham, NC.
4. MJ More, MB Williams, D Narayanan, S Majewski, D Kieper. X-ray Stereotactic Lesion Localization in Conjunction With Dedicated Scintimammography. IEEE Medical Imaging Conference, November 12-16, 2002, Norfolk, VA.
5. MB Williams, D Narayanan, MJ More, PJ Goodale, Analysis of Position-Dependent Compton Scatter in Scintimammography With Mild Compression. IEEE Medical Imaging Conference, November 12-16, 2002, Norfolk, VA.
6. MJ More and MB Williams. Dual Modality Breast Imaging System. Presented at the 21<sup>st</sup> Annual Meeting of The Society for Physical Regulation in Biology and Medicine", January 30-February 1, 2002, San Diego, CA.
7. MB Williams, MJ More, D Narayanan, S Majewski, B Welch, and DA Kieper. Improved Breast Scintigraphy Using Digital Mammography. Conference record, IEEE Nuclear Science Symposium and Medical Imaging Conference, November 7-11, 2001, San Diego, CA.
8. MB Williams, MJ More, S Majewski, R Wojcik, B Kross, V Popov, AG Weisenberger. Dual Modality Breast Imaging. Proc. 1st Topical Symposium on Functional Breast Imaging with Advanced Detectors, April 18-21, 2001, Rome, Italy.
9. MJ More, MB Williams, D Narayanan, S Majewski, D Kieper, and B Kross. Quantification of lesion radioisotope concentration in scintimammography. 1st Topical Symposium on Functional Breast Imaging with Advanced Detectors, April 18-21, 2001, Rome, Italy.
10. MB Williams. Integrated System for Diagnostic Breast Imaging. Presented at the Association for the Advancement of Medical Instrumentation Conference and Exposition, June 10, 2001, Baltimore, MD.
11. MB Williams. Dual Modality Breast Imaging: Structure and Function". presented at the International Conference on Technology in Cancer Research and Treatment in the New Millennium, June 27-30, 2001, Albany NY.

### Related Grant Funding

- 1) The Susan G. Komen Breast Cancer Foundation  
"Dual Modality Imaging for Radioguided Breast Surgery"  
# IMG0402326  
10% time commitment  
5/1/04 - 4/30/06

### Graduate Degrees Supported by This Award

Patricia J. Goodale, PhD, Engineering Physics

Mitali J. More, PhD Biomedical Engineering

Deepa Narayanan, MS Biomedical Engineering

### **CONCLUSIONS**

We have developed a new type of dual modality system for breast cancer diagnosis. The device constitutes an integrated system for combining functional and structural information regarding normal and pathological breast structures. The system has demonstrated the ability to provide unambiguous correlation between structures in the structural (x-ray) and functional (gamma ray) images. Upgrading of scanner components and associated software has resulted in a more accurate and versatile scanner. Basic studies using phantoms have pointed to the value of mild breast compression for increasing lesion contrast. In addition, our studies have pointed to the importance of optimization of image acquisition strategy based on the location of the lesion within the breast. Characterization of the scatter radiation contributing to the gamma image has shown a distinct correlation between breast thickness and the amount of scatter. Early results of a clinical evaluation of the scanner, using histologic findings as ground truth, are very promising. Ongoing work, including multiple view acquisition, is likely to further enhance the diagnostic capabilities of the system. It is anticipated that, compared to current non-integrated imaging procedures, breast lesions that are smaller and of a wider variety can ultimately be reliably characterized.

# Phantom Study of Radiotracer Concentration Quantification in Breast Scintigraphy

Mark B. Williams, *Member, IEEE*, Mitali J. More, Deepa Narayanan, Stan Majewski, Ben Welch, Randolph Wojcik, and Douglas A. Kieper

**Abstract**—The authors are developing a breast imaging system that combines digital X-ray mammography and gamma emission scintigraphy in an integrated unit. One potential value of such a combination is the ability to quickly obtain information about breast shape and lesion position within the breast via X-ray and then to use this information to perform corrections to the gamma image(s). In particular, the effects of gamma ray attenuation, gamma camera resolution, and scatter can be taken into account so as to better estimate the difference between the image contrast and true radioactivity contrast. The authors present results of a phantom study designed to test how well the lesion-to-background contrast can be predicted by this method. The preliminary results indicate that the effects of attenuation, partial volume averaging, and scatter on lesion image contrast can be modeled and suggest that the model might be usefully employed in the dual modality breast scanner to correct the breast scintigram for these effects.

**Index Terms**—Digital mammography, multimodal imaging, radioactivity quantification, scintimammography, stereotactic imaging.

## I. INTRODUCTION

**B**REAST scintigraphy (scintimammography) is being evaluated as an adjunct modality for X-ray mammography, because it provides functional information complimentary to the structural information found in the mammographic study. We are developing a system for dual modality breast imaging, in which digital mammography images and breast scintigraphy images are obtained in quick succession, with the breast held under mild compression. The X-ray and gamma ray detectors are mounted on a common gantry, and the fact that the breast remains stationary during X-ray and gamma ray image acquisition permits unambiguous correlation between the lesion location in the two images.

For a given true differential radiotracer concentration between lesion and surrounding healthy tissue, the measured signal difference (or contrast) in the scintigram depends strongly on imaging geometry, since attenuation of gamma rays

exiting the lesion, as well as the detector area over which the lesion image is spread, are both functions of the lesion-to-collimator distance [1], [2]. If the location of the lesion within the breast is known, it may be possible to more accurately estimate the relative radiotracer concentration by making explicit corrections for attenuation and camera spatial resolution. Our goal is to use the ability of the X-ray component of the dual modality system to localize the lesion in the breast, thereby permitting these corrections. We present the results of phantom studies demonstrating the feasibility of improved lesion-to-background uptake ratio assessment via this technique.

## II. DUAL MODALITY SYSTEM DESCRIPTION

The digital X-ray and gamma ray detectors are mounted on a conventional upright mammographic unit (Lorad M-III). The digital mammography detector, designed and developed by our group in collaboration with Brandeis University, consists of six butted modules arranged in a  $2 \times 3$  array. Each module contains a  $2 \text{ k} \times 2 \text{ k}$  CCD bonded to the small end of a fiber optic taper. The large ends of the six tapers are optically coupled to a common  $20 \text{ cm} \times 30 \text{ cm}$   $\text{Gd}_2\text{O}_2\text{S}:\text{Tb}$  phosphor. The pixel size is  $0.046 \text{ mm}$ , and a full digital mammogram contains  $4224 \times 6264$  pixels, with 16 bits of intensity resolution per pixel. Performance of the detector in terms of the spatial frequency dependent detective quantum efficiency has been published elsewhere [3].

The dedicated gamma camera of the dual modality breast imaging system consists of 16 tiled Hamamatsu position sensitive photomultiplier tubes (PSPMTs), arranged in a  $4 \times 4$  array. The PSPMT array is optically coupled via acrylic light guides to a  $30 \times 30$  array of  $\text{NaI}(\text{TI})$  crystals from Saint-Gobain. Each crystal is  $3 \text{ mm} \times 3 \text{ mm} \times 6 \text{ mm}$  (thick), and the crystal center-to-center spacing is  $3.3 \text{ mm}$ . The energy resolution is 15% at  $140 \text{ keV}$ . Because of the compact design of the PSPMTs and camera housing, the gamma camera active area extends to within  $8 \text{ mm}$  of the patient's chest wall, a performance comparable to that of X-ray mammography and far superior to that of clinical gamma cameras (at least several cm). The camera uses a high resolution etched tungsten collimator with  $1.25 \text{ mm}$  square apertures (Teconet Corp.), with height  $1.78 \text{ cm}$  ( $1.73 \text{ cm}$  effective length at  $140 \text{ keV}$ ). The collimator septa are  $0.2 \text{ mm}$  thick. The intrinsic detector spatial resolution, averaged over the detector surface, is  $3.8 \text{ mm FWHM}$ . Using a  $-7\%/+22\%$  energy window, the camera sensitivity is  $290 \text{ cpm}/\mu\text{Ci}$  (efficiency of  $1.3 \times 10^{-4}$ ).

The current scanner, now undergoing clinical evaluation, is shown in Fig. 1. In a typical dual modality study, the patient is

Manuscript received November 20, 2001. This work was supported in part by the National Institutes of Health under Grants RO1-CA69452 and RO1-CA66232, by the U.S. Army Breast Cancer Research Program under Grant BC980469, by the Susan G. Komen Foundation under Grant 99-003050, and by Dupont Pharma under Grant GC-97035 and for contribution of the Miraluma used in the clinical studies. The Southeastern Universities Research Association (SURA) operates the Jefferson Lab for the U.S. Department of Energy under Contract DE-AC05-84ER40150.

M. B. Williams, M. J. More, and D. Narayanan are with the University of Virginia, Charlottesville, VA 22908 USA (e-mail: mbwilliams@virginia.edu).

S. Majewski, B. Welch, and R. Wojcik are with the Thomas Jefferson National Accelerator Facility, Newport News, VA 23606 USA.

D. A. Kieper is with Hampton University, Hampton, VA 23668 USA.

Digital Object Identifier 10.1109/TNS.2003.812453

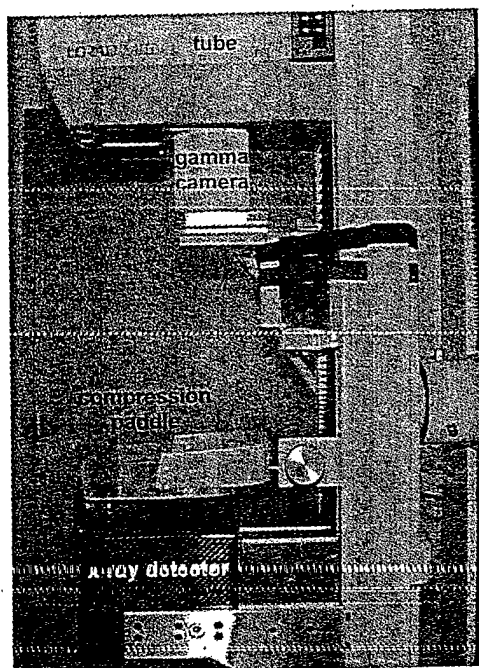


Fig. 1. Dual modality scanner now under clinical evaluation at the University of Virginia. The gamma camera is raised to the location shown for the X-ray image, then lowered to a position immediately above the compression paddle for acquisition of the gamma image.

first positioned in a manner similar to that used in conventional mammography (i.e., with the breast held between the upper surface of the X-ray detector and the compression paddle), except with substantially reduced breast compression. With the gamma camera pivoted out of the path of the X-ray beam a digital mammogram is obtained, and the image appearing on the acquisition monitor is used to verify that the portion of the breast containing the suspicious lesion is approximately centered in the field of view. Next, the gamma camera is swung back into position above the breast and is lowered via a linear translation stage to a position just above the compression paddle. Following acquisition of the gamma emission image ( $\sim 15$  minute acquisition time), the X-ray and gamma ray images are corrected for translational and rotational offsets and their pixel sizes are rescaled to a common value using a stored coregistration file. X-ray and gamma ray images are separately window/leveled, then the common areas of each are fused into a single dual modality image. Details of the procedures for merging the X-ray and gamma ray images are essentially the same as those used in our dual modality small animal scanners and are described elsewhere [4].

In the next generation of scanners now under development, the breast is supported by an independent structure rather than by the X-ray detector. This support structure is mounted on a stainless steel rod that is attached to the generator housing and goes through the gantry arm. Since it is not attached to the gantry arm, the X-ray and gamma ray detectors can rotate independently of the breast. Fig. 2 shows the gantry arm and support structure. The gantry arm is driven by a dc servo motor via a reducing worm gear, permitting rapid reproducible angular displacement of the detectors. Thus, it is possible to obtain multiple views of the breast in a single configuration (no change

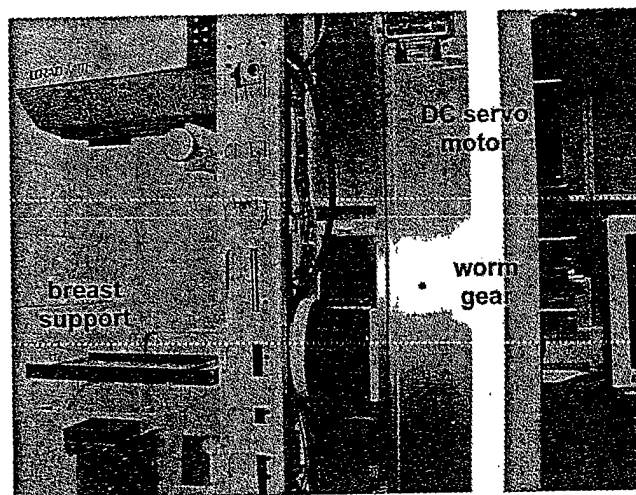


Fig. 2. Dual modality scanner currently under development. The breast support is now independent of the detectors and gantry arm, permitting multiple views of the breast to be obtained. The servo motor and worm gear can be seen to the right of the vertical support frame.

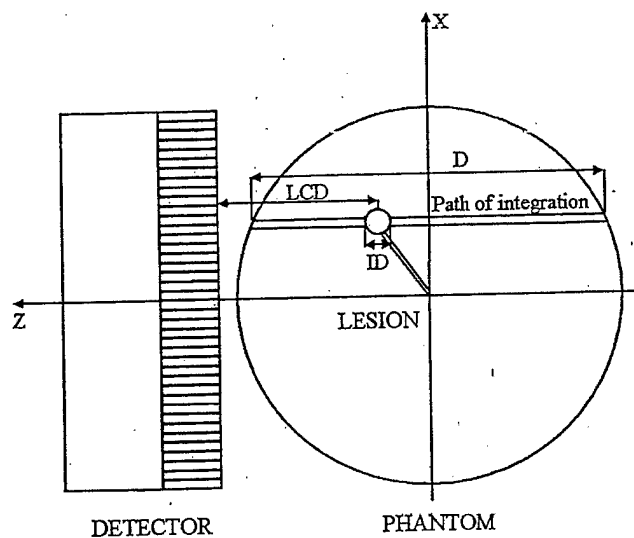


Fig. 3. Schematic diagram of the cylindrical phantom used for the study. One lesion is shown, located at a distance  $LCD$  from the collimator. The length  $D$  is the upper limit in the integral of (1). The inner diameters ( $ID$ ) of the lesions used in the study were 1.0 and 0.8 cm. The view shown is at  $\theta = 0^\circ$ .

in compression orientation) at precisely known angles. By acquiring two X-ray projections of the breast, the lesion can be accurately localized within the breast, as is done on stereotactic breast biopsy systems.

### III. PHANTOM STUDIES

Phantoms containing simulated lesions were constructed to measure the improvement in concentration ratio assessment through lesion localization. Fig. 3 shows a schematic diagram of one such phantom and illustrates the acquisition geometry used in the study. Lesions were attached via low attenuation rods of known length to a central tube. Each rod screwed into one of a set of regularly spaced holes drilled in the tube. The tube was coaxial with an external rod used to mount the phantom on a rotation stage. Thus the tube's axis coincided

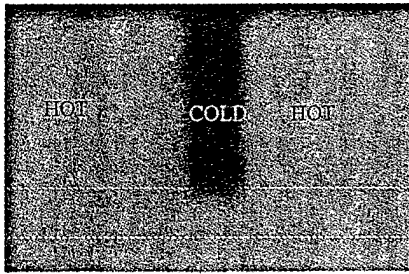


Fig. 4. Image of the phantom used to measure scatter fraction for the lesion contrast studies described.

with the rotation axis (the  $y$  axis in Fig. 3). The radial distance from the phantom center ( $r$ ) and the starting angular position of each lesion relative to the  $+z$  axis ( $\phi$ ) was precisely known based on the rod lengths and location of the holes in the tube. Bends of  $90^\circ$  were made in the rods to minimize superposition of lesions and rods as the phantom was rotated.

For the phantom studies, a gamma camera very similar to that described above was used. The PSPMT and crystal arrays were nominally identical, but in this case the collimator was made of lead, with hexagonal holes with length 2.1 cm (2.0 cm effective length at 140 keV), and inner wall-to-wall dimension of 1.6 mm. Using a  $-8.7\%/+24\%$  energy window, the gamma camera sensitivity was 230 cpm/ $\mu$ Ci (efficiency of  $1.03 \times 10^{-4}$ ), similar to that of the camera with the tungsten collimator. A phantom with a cylindrical cross section was tested. The inner diameter of the phantom was 9.6 cm, and its height was 10.7 cm. Lesions had inner diameters of 8 mm and 10 mm, with outer diameters of 10 mm and 12 mm, respectively. Lesions were obtained from Data Spectrum Corp.<sup>1</sup> Realistic lesion-to-background concentration ratios ( $\sim 6:1$ – $10:1$ ) were used. Gamma images were obtained over a large range of viewing angles,  $\theta$ . Thus the angular offset from the  $z$  axis of the  $i$ th lesion at viewing angle  $\theta$  was ( $\phi_i + \theta$ ). For each view, and for each lesion, slices passing through the lesion were taken from the image.

To quantify the effects of attenuation,  $^{99m}\text{Tc}$  point sources were used to directly measure the attenuation of the acrylic from which the phantoms were constructed. The measured linear attenuation was  $0.18 \text{ cm}^{-1}$ . The measured linear attenuation of water was  $0.16 \text{ cm}^{-1}$ .

Scatter to primary ratios were determined empirically using a phantom the same size as those containing the simulated lesions, but containing a "cold" region (water only). An image of the phantom is shown in Fig. 4. Fig. 5 is a plot of the energy spectra obtained in the hot and cold regions of the phantom. These spectra were used to determine the fraction of total counted events arising from direct (not scattered) gamma rays. For the phantom data presented here, the scatter fraction was 0.32.

Views were obtained by rotating the phantoms on a computer-controlled rotary stage and holding the camera stationary. Acquisition times for each view were adjusted according to the 6 hour half-life of  $^{99m}\text{Tc}$ , so that approximately the same total counts were obtained for each view.

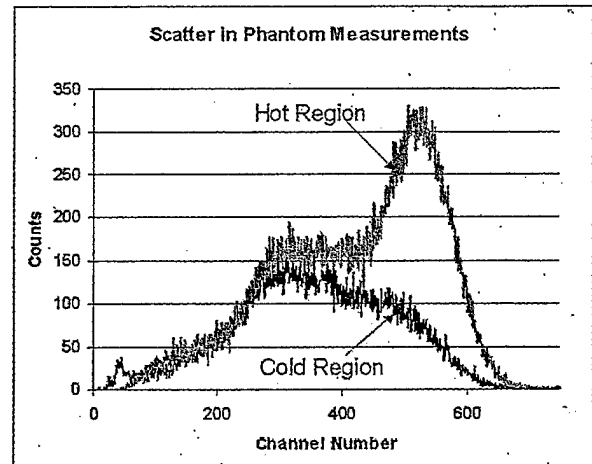


Fig. 5. Spectra obtained using the phantom whose image is shown in Fig. 4. These spectra were used to calculate the scatter fraction for a given energy window.

#### IV. THEORY

Three factors reduce lesion contrast in the images: 1) attenuation of gamma rays radiating from the lesion; 2) partial volume averaging (camera spatial resolution); and 3) scattered gamma rays whose detected energy falls within the energy window used for acquisition. We define  $n_L$  as the number of counts in a lesion pixel, and  $n_b$  as the number of counts in a background pixel. Theoretical expressions for  $n_L$  and  $n_b$  that include the effects of gamma camera spatial resolution, attenuation, and scatter are obtained as follows.

The total number of counts in a pixel in the image is given by

$$n = \epsilon t A_{\text{wall}} p^2 \int_0^D C(z) e^{-\mu_w z} dz \quad (1)$$

where  $\epsilon$  is the detection efficiency,  $t$  is the acquisition time,  $A_{\text{wall}}$  is the attenuation due to the acrylic wall on the camera side of the phantom,  $p$  is the pixel size,  $C(z)$  is the activity per unit volume,  $D$  is the thickness of the phantom above the pixel, and  $\mu_w$  is the linear attenuation coefficient of water for 140 keV gamma rays. Note that by using  $\mu_w$  only in (1), we have ignored the difference between the linear attenuation of water and that of the walls of the lesions, even though some detected gamma rays are emitted from background regions behind a lesion. This is reasonable since the lesion walls are thin ( $\sim 1$  mm) compared to the overall phantom dimensions ( $\sim 9$ – $15$  cm). Thus, for a pixel viewing the background region of the phantom, relative to the zero attenuation case, the reduction in counts due to attenuation is given by

$$\frac{n_{\mu \neq 0}}{n_{\mu = 0}} = \frac{A_{\text{wall}} [1 - \exp(-\mu_w D)]}{\mu_w D} \quad (2)$$

The total number of image counts due to gamma rays coming from the lesion is given by

$$N_{L,\text{total}} = C_L V_L t \epsilon A \quad (3)$$

where  $C_L$  is the activity concentration in the lesion,  $V_L$  is the lesion volume,  $t$  is the acquisition time,  $\epsilon$  is the gamma camera

<sup>1</sup>Hillsborough, NC, USA.

efficiency, and  $A$  is the attenuation of the water and acrylic lying between the lesion and the gamma camera.

To take into account the reduction in contrast due to camera blur, we calculate the shape of the lesion's projection onto the detector, convoluted with the camera's two-dimensional (2-D) point spread function (PSF). With no blur, the 2-D count density function of the image of a spherical lesion, projected onto a the surface of the detector, has the form

$$N_L(x, y) = 0 \text{ for } \frac{|x'|^2 + |y'|^2}{R^2} \geq 1$$

$$= N_{L, \max} \left\{ 1 - \left[ \frac{|x'|^2 + |y'|^2}{R^2} \right] \right\}^{1/2}$$

$$\times \text{for } \frac{|x'|^2 + |y'|^2}{R^2} < 1 \quad (4)$$

where  $R$  is the lesion radius,  $x_L$  and  $y_L$  are the  $x$ - and  $y$ -coordinates of the lesion center,  $x' \equiv x - x_L$ ,  $y' \equiv y - y_L$ , and the peak amplitude  $N_{L, \max}$  is set by the condition

$$\iint N_L(x, y) dx dy = N_{L, \text{total}} \quad (5)$$

In these phantom studies, the lesion-to-collimator distance (LCD) is a function of the phantom rotation angle, as is the location,  $x, y$ , on the collimator surface onto which the image of the lesion projects (see Fig. 3). Including detector blur, lesion profile is given by the convolution of the projected sphere profile  $N_L(x, y)$  and the 2-D Gaussian PSF

$$N_{L, \text{blur}}(x, y) = N_L(x, y) \otimes g(x, y)$$

$$\text{where } g(x, y) = \exp \left( -\frac{(x - x_L)^2 + (y - y_L)^2}{2\sigma^2} \right) \quad (6)$$

where  $\sigma$  is equal to the full-width at half-maximum (FWHM) of the camera LSF divided by 2.355.

To find  $\sigma$  as a function of LCD, the line response function (LSF) of the gamma camera was measured over a range of source-to-collimator distance ranging from the minimum to maximum LCD values used in the phantom study. A thin ( $\sim 1$  mm inner diameter) capillary tube filled with  $^{99m}\text{Tc}$  solution was used to produce a line source input. The capillary was angled relative to the rows and columns of the detector crystal array so that the phase relationship between the line input and the crystal sampling matrix varied over the length of the imaged line. Camera resolution for each capillary-to-collimator distance was computed as the FWHM of the image of the capillary, averaged over its length. Fig. 6 shows the measured FWHM camera resolution. Profiles made through the line source images indicated that the camera LSF is well represented by a Gaussian function.

Convolution with the 2-D Gaussian PSF broadens the shape of  $N_{L, \text{blur}}(x, y)$  with respect to that of  $N_L(x, y)$ . The requirement that

$$\iint N_{L, \text{blur}}(x, y) dx dy = N_{L, \text{total}} \quad (7)$$

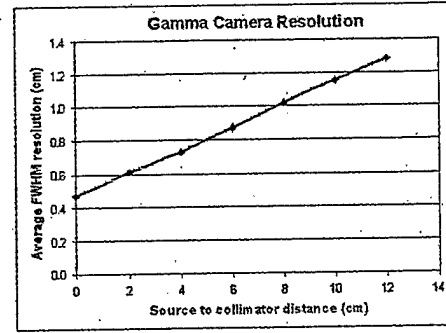


Fig. 6. Measured FWHM gamma camera spatial resolution as a function of the source-to-collimator distance. Values shown represent the resolution averaged over the surface of the camera.

corresponds physically to the requirement that the total number of counts in the blurred profile equals that in the unblurred profile. This requirement sets the amplitude of  $N_{L, \text{blur}}(x, y)$ .

The image contrast with and without scatter radiation is

$$C = \frac{n_L - n_b}{n_b}; C_s = \frac{(n_L + n_s) - (n_b + n_s)}{n_b + n_s} \quad (8)$$

where  $n_L$ ,  $n_b$ , refer to the number of counts in a pixel at the center of the lesion image, and in the background, respectively, and  $n_s$  refers to the additional counts from scatter. Here, we make the reasonable assumption that the number of scatter counts in a lesion pixel is approximately equal to that in a background pixel.

Equation (8) indicates that the reduction in contrast due to scattered radiation is

$$\frac{C_a}{C} = \frac{n_b}{n_b + n_s} = 1 - \frac{n_s}{n_b + n_s} \quad (9)$$

The ratio  $n_s/(n_b + n_s)$  (the scatter fraction) was determined from the spectra shown in Fig. 5, using the energy window utilized for image acquisition. This permits  $n_s$  to be determined for any given value of  $n_b$  calculated from scatter-free conditions.

The theoretical value for the number of counts in a background pixel is obtained by using (1). The theoretical value for the number of counts in the center pixel of the lesion image is obtained by using (3)–(7) to obtain the peak amplitude of  $N_{L, \text{blur}}(x, y)$ . This peak amplitude gives the quantity  $(n_L - n_b)$ . Then (8) and (9) are used to obtain the calculated image contrast.

## V. IMAGE ANALYSIS

To quantify the effects of attenuation, spatial resolution, and scatter in the phantom image data, the phantom images were analyzed as follows. First, for each lesion, a row of pixels going through the lesion center was extracted. Next several rows near the first row, but containing only background were extracted. The background-only rows were averaged to obtain a background-only row in the region of the lesion. This averaged background-only row was then subtracted from the row containing the lesion on a pixel-by-pixel basis. The resulting difference row contains only the profile of the lesion and noise. For simplicity, a Gaussian function was fit to the profile to obtain a noise-free estimate of the peak amplitude. For the (small) lesion sizes and (relatively large) lesion-to-collimator distances used in

TABLE I  
PARAMETERS FOR PHANTOM IMAGE ACQUISITION

Quantity	Symbol	Units	Value
Camera detection efficiency	$\epsilon$	dimensionless	$1.03 \times 10^{-4}$
Background activity concentration	$C_b$	$\mu\text{Ci}/\text{cm}^3$	1.4
Lesion activity concentration	$C_L$	$\mu\text{Ci}/\text{cm}^3$	14.5
Acquisition time per view	$t$	seconds	1200 seconds for first view, decay corrected thereafter
Pixel area	$A_p$	$\text{cm}^2$	0.11
Scatter fraction	SF	dimensionless	0.32
Lesion-to-collimator distance	LCD	cm	~ 4 (minimum) ~ 9 (maximum)

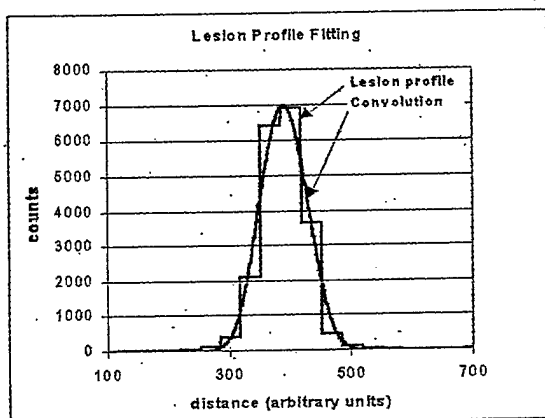


Fig. 7. Plots of experimentally determined lesion profile (straight line segments), and the function  $P_L$  (smooth curve), given by the convolution of (3).

this study, a Gaussian function was a reasonable fit to the measured lesion profile. The peak amplitude of the fit, along with the pixel value in the corresponding pixel of the averaged background-only row, were used to calculate the measured image contrast.

## VI. RESULTS

Table I summarizes the parameter values used in the acquisition. Fig. 7 shows an example of a profile through a lesion phantom, along with a slice through the center of the convolution defined in (6). The particular example shown is for  $R = 0.5$  cm and  $\sigma = 0.27$  cm. Although the relatively small lesion size causes its image to be spread over a small number of pixels, the figure shows that the lesion profile is well fit by the expression of (6). Figs. 8–10 are plots of the measured and calculated values for  $n_b + n_s$ ,  $n_L + n_s$ , and the contrast, for a study using the cylindrical phantom. Views were obtained at  $15^\circ$  intervals over  $345^\circ$ .

The errors in the predicted values, relative to the measured values are given in Table II.

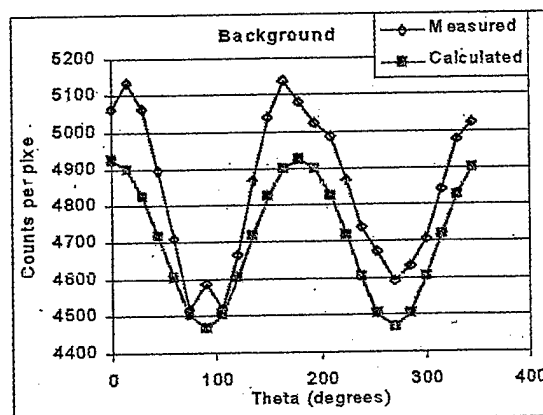


Fig. 8. Measured and calculated values of  $n_b + n_s$  near one of the lesions in the cylindrical phantom. Views were obtained over  $345^\circ$ , with  $15^\circ$  between views. The minimum LCD, at  $\theta = 0^\circ$ , was 3.85 cm, and the maximum LCD, at  $\theta = 180^\circ$ , was 9.15 cm.

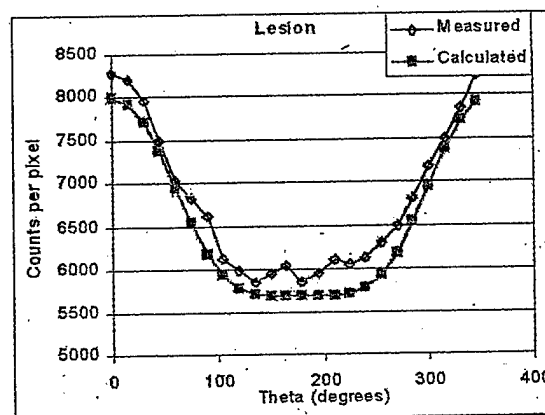


Fig. 9. Measured and calculated values of  $n_L + n_s$  for one of the lesions in the cylindrical phantom. Views were obtained over  $345^\circ$ , with  $15^\circ$  between views. The minimum LCD, at  $\theta = 0^\circ$ , was 3.85 cm, and the maximum LCD, at  $\theta = 180^\circ$ , was 9.15 cm.

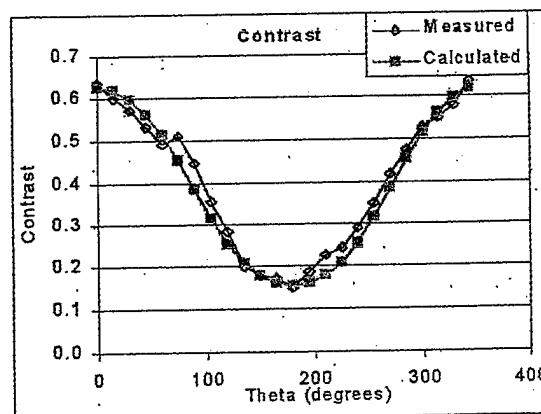


Fig. 10. Measured and calculated values of lesion image contrast for the lesion whose data are shown in Figs. 8 and 9. Views were obtained over  $345^\circ$ , with  $15^\circ$  between views.

## VII. DISCUSSION AND CONCLUSION

The above results indicate that the theoretical construct models the true effects from attenuation, spatial resolution, and scatter with reasonable accuracy. In these studies, the lesion

TABLE II  
AVERAGE ERROR AND RMS DEVIATION IN THE ERROR, OVER 345°, OF  
THE QUANTITIES PLOTTED IN FIGS. 8-10

Quantity	Average Error (%)	Standard Deviation
$n_b + n_s$	2.8	1.1
$n_L + n_s$	3.9	1.6
Contrast ( $n_L - n_b / n_b + n_s$ )	4.8	7.6

location, lesion size, attenuating thickness of overlying breast tissue, lesion-to-collimator distance, and scatter-to-primary ratio were known *a priori* from known phantom dimensions and direct measurement of scatter. In a clinical context, the breast shape will be determined from the X-ray images and the compressed breast thickness. The lesion size can be estimated based on both the X-ray and gamma ray images. The scatter-to-primary ratio is a function of the location in the breast and increases with decreasing distance to the chest wall. In our current dual modality breast scanner, we routinely compile energy spectra for several separate contiguous regions going between the chest wall and anterior edges of the detector. These spectra could be used to estimate the scatter-to-primary ratio at a given location within the breast. Thus, if the location within the breast of the lesion is known, these formalisms can be used to correct the measured (image) contrast so that it is closer to the true (radioisotope) contrast. The use of multiple view X-ray imaging in the dual modality system will permit this localization to be made prior to gamma image acquisition. It is anticipated that such techniques may improve quantification of radiotracer uptake in scintimammography.

There are several challenges to clinical implementation of this approach. First, there will be a certain number of cases in which localization of the lesion and estimation of its size via X-ray may be difficult because of surrounding radiodense breast tissue. One possible solution for such cases is to obtain lesion position information from stereoscopic gamma images. Second, regional variations in scatter-to-primary ratio within the breast may make estimation of the scatter fraction in the region of the lesion difficult. We are currently assessing the magnitude and nature of these variations in data obtained in our ongoing planar dual modality clinical study. Third, the background radiotracer is likely to vary within the breast, due to normal differences in uptake between various tissues. This will make assessment of the contrast dependent on the region of the image chosen for measurement of the quantity  $n_b + n_s$ .

#### REFERENCES

- [1] I. N. Weinberg, R. Pani, R. Pellegrini, F. Scopinaro, G. De Vincentis, A. Pergola, and A. Soluri, "Small lesion visibility in scintimammography," *IEEE Trans. Nucl. Sci.*, vol. 44, pp. 1398-1402, 1997.
- [2] S. Majewski, D. Kieper, E. Curran, C. Keppel, B. Kross, A. Palumbo, V. Popov, A. G. Weisenberger, R. Welch, R. Wojcik, M. B. Williams, M. More, and G. Zhang, "Optimization of dedicated scintimammography procedure using detector prototypes and compressible phantoms," *IEEE Trans. Nucl. Sci.*, vol. 3, pp. 822-829, 2001.
- [3] M. B. Williams, P. U. Simoni, L. Smilowitz, M. Stanton, and W. Phillips, "Analysis of the detective quantum efficiency of a developmental detector for digital mammography," *Med. Phys.*, vol. 26, pp. 2273-2285, 1999.
- [4] M. B. Williams, V. Galbis-Reig, A. Goode, P. Simoni, S. Majewski, A. Weisenberger, R. Wojcik, W. Phillips, and M. Stanton, "Dual modality system for small animal imaging," *RSNA Electron. J.*, vol. 3, 1999.



# Analysis of Position-Dependent Compton Scatter in Scintimammography With Mild Compression

Mark B. Williams, *Member, IEEE*, Deepa Narayanan, Mitali J. More, Patricia J. Goodale, Stan Majewski, Douglas Kieper

**Abstract**— In breast scintigraphy using  $^{99m}\text{Tc}$ -sestamibi the relatively low radiotracer uptake in the breast compared to that in other organs such as the heart results in a large fraction of the detected events being Compton scattered gamma rays. In this study, our goal was to determine whether generalized conclusions regarding scatter-to-primary ratios at various locations within the breast image are possible, and if so, to use them to make explicit scatter corrections to the breast scintigrams. Energy spectra were obtained from patient scans for contiguous regions of interest (ROIs) centered left to right within the image of the breast, and extending from the chest wall edge of the image to the anterior edge. An anthropomorphic torso phantom with fillable internal organs and a compressed-shape breast containing water only was used to obtain realistic position-dependent scatter-only spectra. For each ROI, the measured patient energy spectrum was fitted with a linear combination of the scatter-only spectrum from the anthropomorphic phantom and the scatter-free spectrum from a point source. We found that although there is a very strong dependence on location within the breast of the scatter-to-primary ratio, the spectra are well modeled by a linear combination of position-dependent scatter-only spectra and a position-independent scatter-free spectrum, resulting in a set of position-dependent correction factors. These correction factors can be used along with measured emission spectra from a given breast to correct for the Compton scatter in the scintigrams. However, the large variation among patients in the magnitude of the position-dependent scatter makes the success of universal correction approaches unlikely.

**Index Terms**— breast imaging, Compton scatter, multimodality, scintimammography

## I. INTRODUCTION

During the past several years, we have been developing a breast scanning system that combines digital x-ray mammography with breast scintigraphy using a dedicated small field of view gamma camera [1]. The x-ray and gamma ray detectors are mounted on an upright mammography

gantry, and the x-ray transmission and gamma emission views are obtained sequentially while the breast is held in a fixed configuration using mild compression. The chest wall edges of the x-ray and gamma ray detectors coincide, and the gamma camera is centered left-to-right within the field of view of the x-ray detector. The fields of view of the gamma camera and x-ray detector are 10 cm x 10 cm and 19 cm x 28 cm, respectively. In an ongoing clinical evaluation, the resulting dual modality images have proven effective for differentiation of benign and malignant breast masses, compared to prone scintimammography alone, with our dedicated camera.

The presence of counts in the gamma image due to Compton scattered gamma rays can reduce lesion contrast [2]. In this study, our goal was to determine whether generalized conclusions regarding scatter-to-primary ratios at various locations within the image are possible, and if so, to use them to make explicit scatter corrections. In a typical gamma image acquisition using the dual modality system, a two-dimensional image histogram is updated each time a gamma interaction occurs that deposits an amount of energy in the detector that falls within a predetermined energy window. However, in a number of recent patient studies, gamma emission data were acquired in list mode rather than in the conventional single histogram mode. In list mode, the location on the detector surface of the gamma ray interaction, the time at which the interaction occurred, and the total energy of the interaction are stored individually for each detected gamma event. The resulting list of x, y, t, and E values can then be replayed with any desired energy discrimination criteria. In addition, energy spectra corresponding to any arbitrary region of the detector surface may be obtained. We have used this capability to study the spatial dependence of the Compton scatter coming from the breast.

## II. METHODS

### A. Imaging System

The dual modality breast imaging system at the University of Virginia consists of a digital x-ray detector and a dedicated gamma camera mounted on a single upright unit (Lorad MIII). The x-ray detector, built at Brandeis University, Waltham, MA, consists of six butted modules arranged in a 2 x 3 array. Each module contains a 2k x 2k CCD bonded to the small end of a 3.3:1 fiber optic taper. The large ends of the six tapers are optically coupled to a common 20 cm x 30 cm  $\text{Gd}_2\text{O}_2\text{S:Tb}$  phosphor. The pixel size is 46 microns, and a full digital

Manuscript received November 20, 2002. This work was supported in part by grants from the National Institutes of Health (grants RO1 CA69452 and RO1 CA66232), the US Army Breast Cancer Research Program (grant BC980469) and the Susan G. Komen Foundation (grant 99-003050). We also wish to thank Dupont Pharma, for contribution of the Miraluma used in the clinical studies (grant GC 97035).

M. B. Williams, M. J. More, D. Narayanan and P. J. Goodale are with the University of Virginia, Charlottesville, VA 22908 USA (telephone: 434-982-4422, e-mail: mbwilliams@virginia.edu).

S. Majewski is with the Thomas Jefferson National Accelerator Facility, Newport News, VA 23606 USA. The Southeastern Universities Research Association (SURA) operates the Jefferson Lab for the United States Department of Energy under contract DE-AC05-84ER40150.

D. A. Kieper is with Hampton University, Hampton, VA 23668 USA.

mammogram contains 4224 x 6264 pixels, with 16 bits per pixel. The inactive border at the chest wall edge is 7 mm wide.

The dedicated gamma camera of the dual modality breast imaging system, built at the Thomas Jefferson National Accelerator Facility (TJNAF), is mounted on the same gantry and is moved out of the way while acquiring the x-ray image. The gamma camera consists of a 4 x 4 array of one inch square position sensitive photo multiplier tubes (PSPMTs) (Hamamatsu R7600-00-C8). The PSPMT array is optically coupled via acrylic light guides to a 30 x 30 array of NaI(Tl) crystals. Each crystal is 3.0 mm x 3.0 mm x 6 mm thick, and the crystal center-to-center spacing is 3.3 mm. Because of the compact design of the PSPMTs and camera housing, the gamma camera is able to image to within 8 mm of the patient's chest wall. The camera uses a high-resolution etched tungsten parallel hole collimator with square apertures. The single crystal energy resolution is ~15% at 140 keV. Images are typically obtained using a +22/-7% energy window set around the 140 keV photopeak of  $^{99m}\text{Tc}$ .

### B. Patient Imaging

During the past three years, the dual modality system has been used in a clinical study conducted at the Primary Care Center at the University of Virginia to test its ability to distinguish between malignant and benign lesions [1]. Participants are recruited from patients who have already undergone screening mammograms and are scheduled for biopsy.

For this study, the patient is given an intravenous injection of 25-30 mCi of  $^{99m}\text{Tc}$ -sestamibi in the arm contralateral to the suspicious breast. The suspicious breast is then positioned on the x-ray detector. The compression paddle provides mild compression to maintain a consistent breast configuration for both imaging modalities. An x-ray image is obtained to confirm that the suspicious lesion will be within

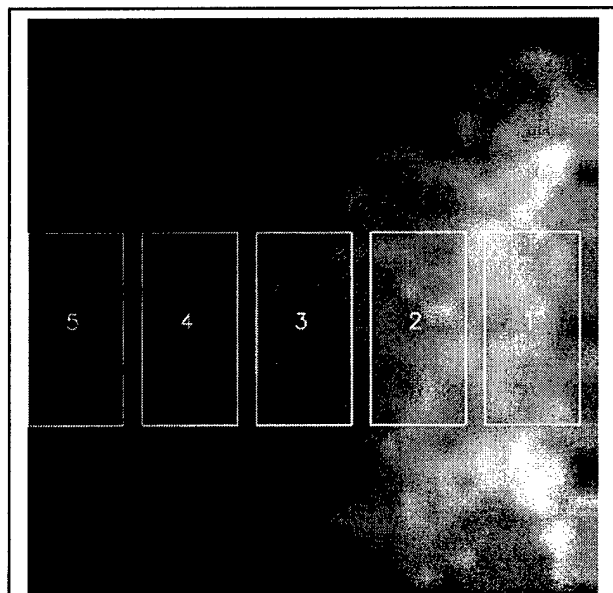


Fig. 1. Example patient gamma image showing five ROIs, going from the chest wall edge of the image to the anterior edge, along the midline of the breast.

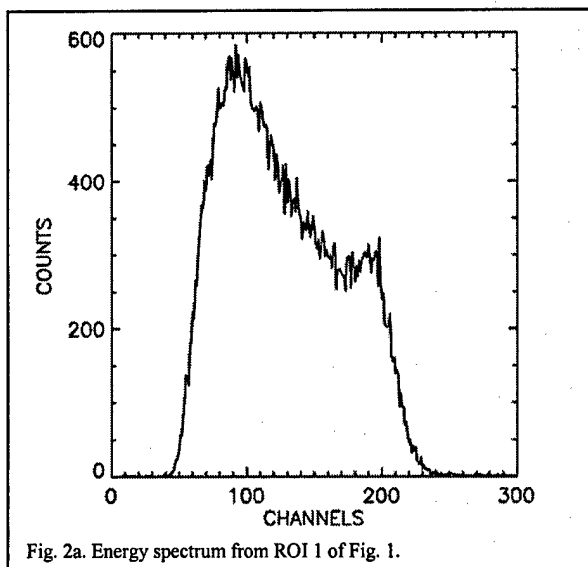


Fig. 2a. Energy spectrum from ROI 1 of Fig. 1.

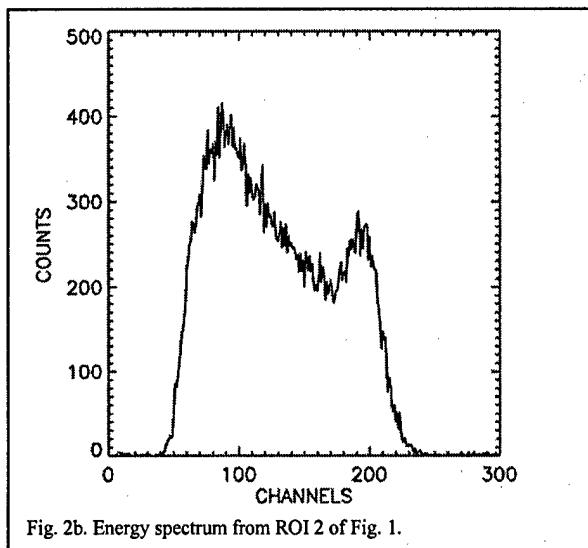


Fig. 2b. Energy spectrum from ROI 2 of Fig. 1.

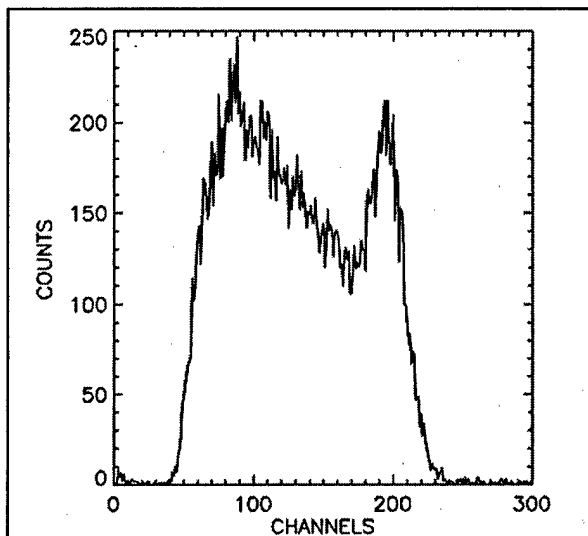
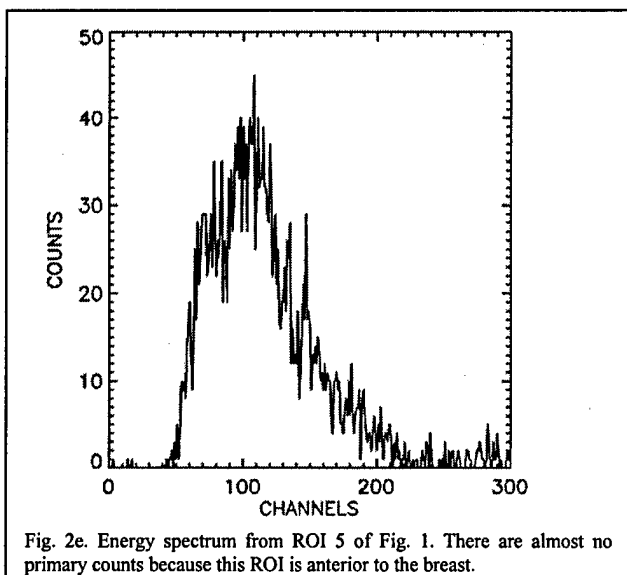
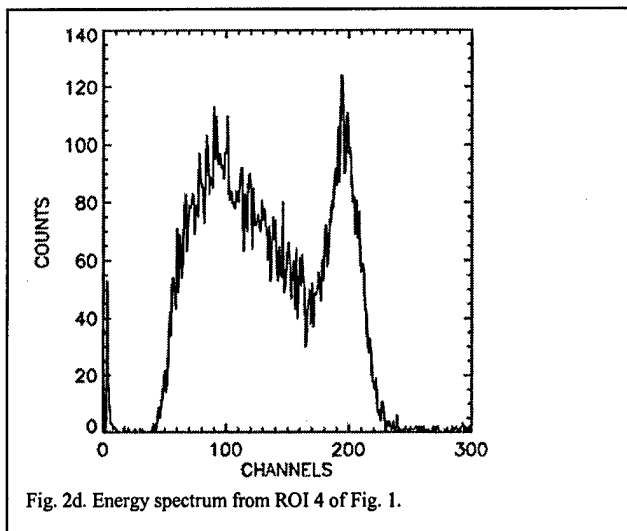


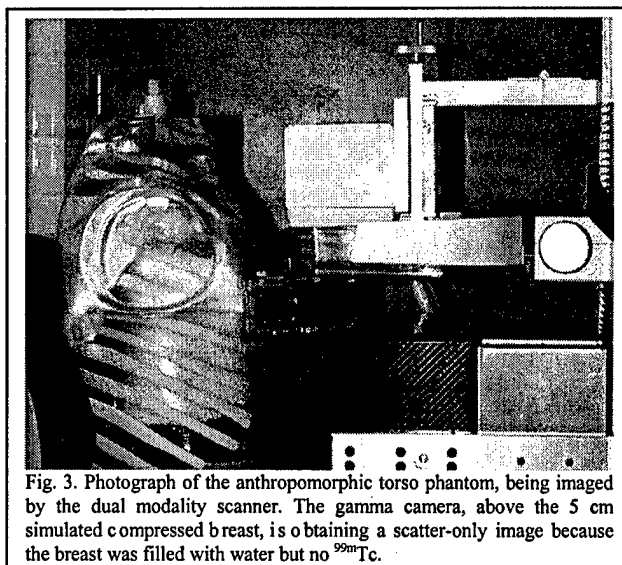
Fig. 2c. Energy spectrum from ROI 3 of Fig. 1.



the 10 cm x 10 cm field of view of the gamma detector when it is swung into position. Gamma image acquisition is begun once correct location of the lesion in the x-ray image is verified. The typical acquisition time is ~10-15 minutes. The above procedure (x-ray and gamma ray imaging) is then performed on the non-suspicious breast. For the studies described here, acquisition was done in list mode, whereby the time, position, and energy of each gamma interaction in the detector is stored. The threshold setting for the discriminator gating the ADCs was set just above the electronic noise, so that the entire energy spectrum was recorded.

### C. Image Analysis

Individual energy spectra were obtained for each of five contiguous 3.3 cm x 2 cm regions of interest (ROIs) in the gamma images of both breasts of each patient. The ROIs were centered left to right in the image, and extended from the chest wall edge of the image to the anterior edge (see Fig. 1). ROI 5 is the region farthest from the chest wall edge while ROI 1 is the region closest to the chest wall edge. Fig. 2(a)-(e) shows the energy spectra for each of the five ROIs are shown in Figs.



2a)-e). The horizontal axes of the spectra are normalized so that channel 200 corresponds to 140 keV. As we go from ROI 5 to 1, in the direction towards the chest wall, we see that the height of scatter peak increases relative to that of the primary peak. The spectrum from ROI 5 has few primary (photopeak) counts because in this example the breast does not extend into that part of the image. It is apparent from the spectra that even with a -7% lower energy level, some scatter is likely to be present in the image, particularly in regions near the chest wall. Overlap between photopeak counts and scatter counts makes it very difficult to directly correct for the unwanted scatter counts. Therefore, our objective was to decompose the spectra into their primary and scatter components, so that the scatter fraction could be estimated.

### D. Emission Spectra Decomposition

We model the clinical breast emission spectra as a linear combination of a scatter-free spectrum and a scatter-only spectrum. That is, for the  $i^{\text{th}}$  ROI, the emission spectrum is:

$$S_i = a_{0,i} S_p + a_{1,i} S_{s,i} \quad (1)$$

where  $a_{0,i}$  and  $a_{1,i}$  are spatially varying coefficients that scale the scatter-free spectrum,  $S_p$ , and scatter-only spectrum,  $S_{s,i}$  respectively.

The scatter-free spectrum is that from a point source of  $^{99m}\text{Tc}$ , and is independent of position in the image.

The scatter-only spectrum varies strongly from one location to another, as can be readily seen in Figs. 2(a)-e). To obtain estimates of the scatter-only spectra, we used an anthropomorphic torso phantom with individually fillable internal organs and torso (Radiological Support Devices, Long Beach, CA). For this study, externally attached breasts with uniform thickness (5 cm) in the cranio-caudal direction were used to simulate compressed breasts. The radioactivity concentrations used in the various phantom regions are given in Table I. The activity concentration distribution used was based on the bio-distribution of  $^{99m}\text{Tc}$ -sestamibi at 5 minutes post injection [3].

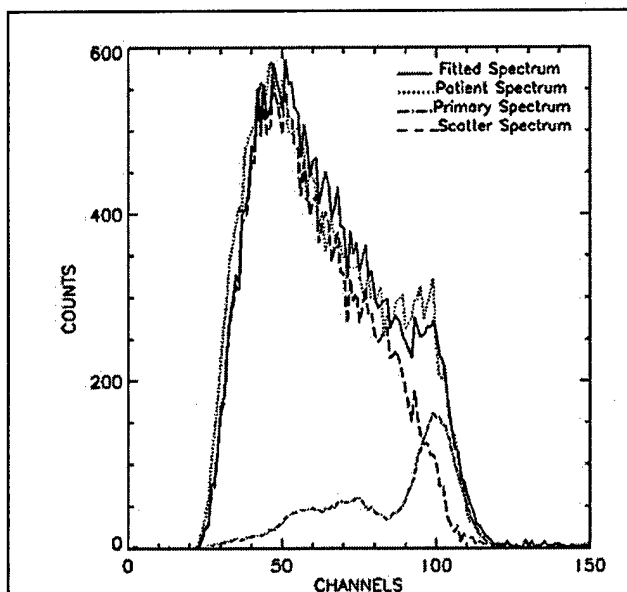


Fig. 4a. Energy spectrum from ROI 1, (Patient spectrum) along with the scaled primary and scatter-only spectra, and their sum (Fitted spectrum).

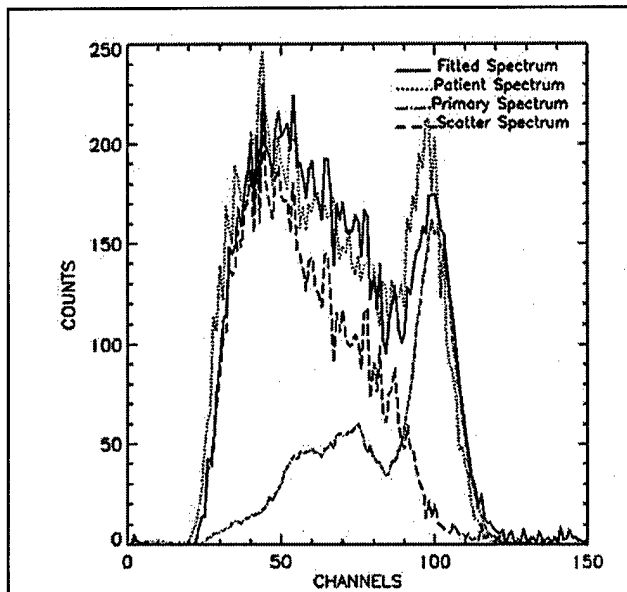


Fig. 4c. Energy spectrum from ROI 3, along with the scaled primary and scatter-only spectra, and their sum.

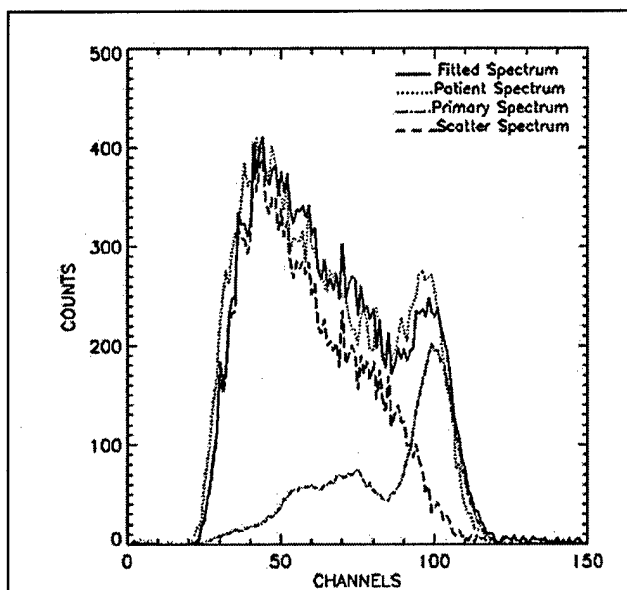


Fig. 4b. Energy spectrum from ROI 2, along with the scaled primary and scatter-only spectra, and their sum.

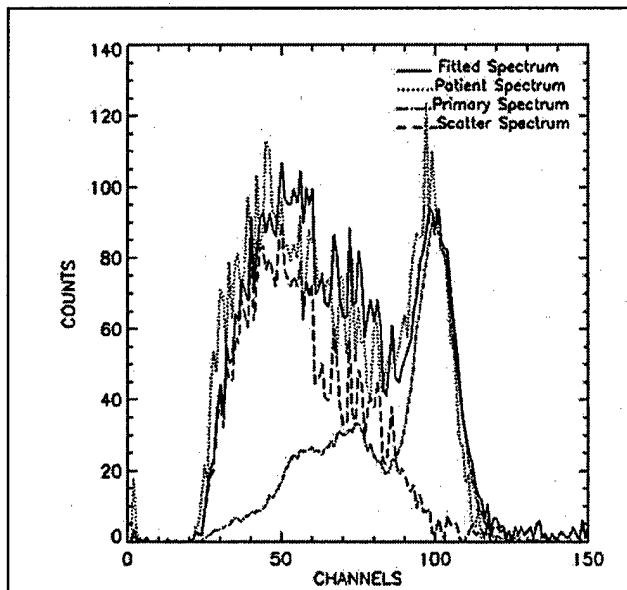


Fig. 4d. Energy spectrum from ROI 4, along with the scaled primary and scatter-only spectra, and their sum.

The anthropomorphic torso phantom was scanned using the dual modality breast scanner and the same positioning as was used for the clinical scans, although no x-ray images were obtained. Fig. 3 is a photograph of the setup. Emission spectra were obtained from the anthropomorphic phantom breasts using the same ROIs as shown in Fig. 1. Using these spectra as the  $S_{s,i}$  of (1) and the spectra obtained from the point source as  $S_p$ , the coefficients  $a_0$  and  $a_1$  were found for each of the five ROIs using a least-squares curve fitting routine that minimizes the error between the expression in (1) and the measured clinical emission spectrum,  $S_c$ . The criterion used to

establish goodness of fit was that the relative decrease in chi-squared value from one iteration of the curve fitting routine to the next was less than  $1.1 \times 10^{-3}$ . Figs. 4a) – 4e) show the fits to the example clinical spectra of Fig. 2. For each of the five ROIs, the patient spectrum, the fitted spectrum  $S$ , and its components  $a_0 S_p$  and  $a_1 S_s$  are shown.

The position-dependent scatter fraction, defined as the ratio of scatter counts to total counts, was then obtained as follows. For a selected energy window, the number of counts in the scaled scatter-only spectrum ( $a_1 S_s$ ) falling within the energy window was determined. The ratio of this number to the total number of counts in the original patient spectrum

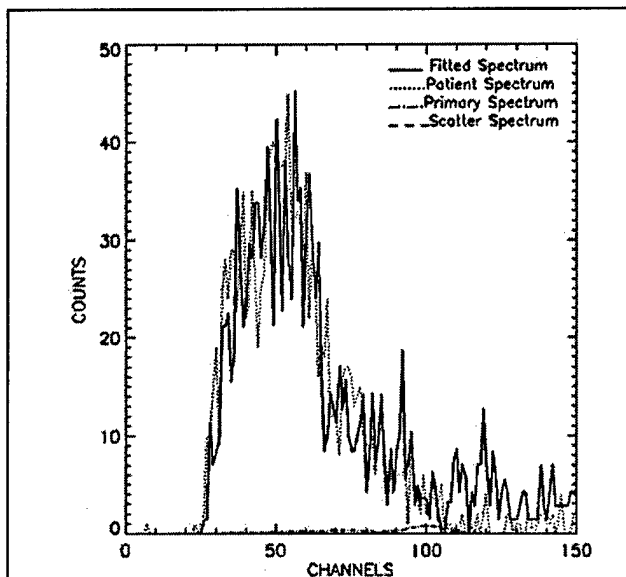


Fig. 4e. Energy spectrum from ROI 5, along with the scaled primary and scatter-only spectra, and their sum.

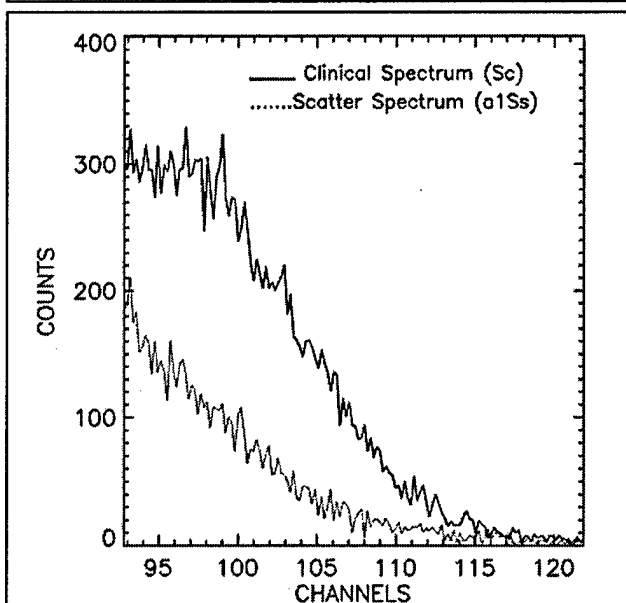


Fig. 4f. Expanded view of the  $-7\%/+22\%$  energy window (channel 512 corresponds to 140 keV), showing the portions of the spectra  $S_c$  and  $a_1S_s$  falling within the window for ROI 4.

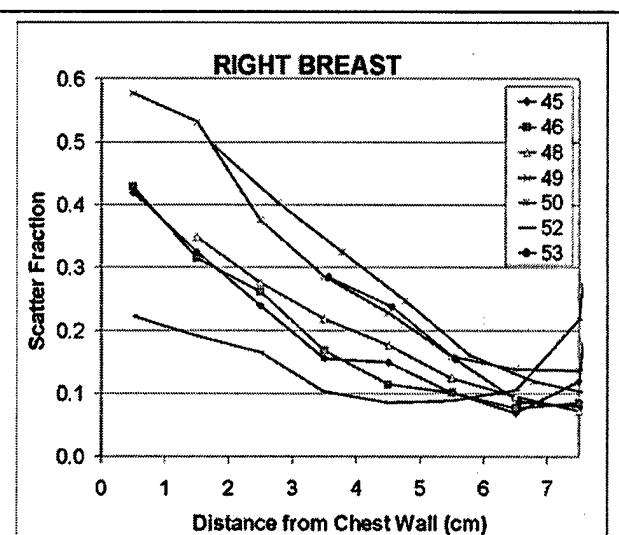
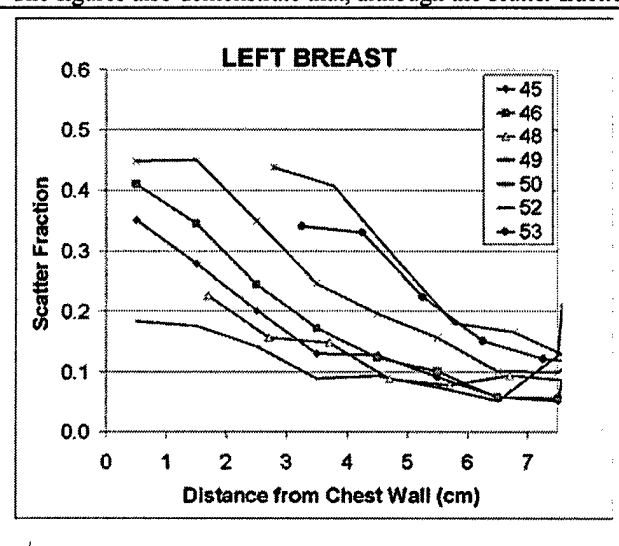
falling within the energy window is the scatter fraction. Fig. 4f shows an expanded view of the  $+22\%/-7\%$  energy window, with the portions of  $a_1S_s$  and  $S_c$  that fall within it in ROI 4. The scatter fraction is the ratio of the area under the  $a_1S_s$  curve to that under the  $S_c$  curve.

Once the scatter fractions for each ROI have been calculated, the images are scatter corrected as follows. The scatter fraction for each ROI is attributed to the pixel at its center. Linear interpolation in the chest-anterior direction is used to estimate scatter fractions for the other pixels. We assume a constant scatter fraction in the left-right direction (see Fig. 7). Each pixel is scatter corrected by subtracting a

number of counts equal to its uncorrected count times the scatter fraction for that pixel.

### III. RESULTS

We have characterized the spatial dependence of the scatter fraction in eleven cases (twenty-two dual modality breast scans). Figs. 5 and 6 are plots of the scatter fraction versus the distance in centimeters from the chest wall, for cranio-caudal views of the left and right breasts, respectively, of seven patients. The ROIs in which the scatter fractions were measured were  $2.0\text{ cm} \times 3.3\text{ cm}$  ( $6 \times 10$  pixels), and were placed along the midline of the breast. The plots show that for each case, there is a distinct decrease in the scatter fraction with increasing distance from the chest wall. In the case of patient 52, the scatter fraction increases sharply beyond 6.5 cm from the chest wall because in that particular case the compressed breast only extended  $\sim 6$  cm from the chest wall. The figures also demonstrate that, although the scatter fraction



Figs. 5 and 6. Scatter fraction versus distance from the chest wall in the left and the right breast. Curves are labeled according to case number, with data points connected by lines for clarity.

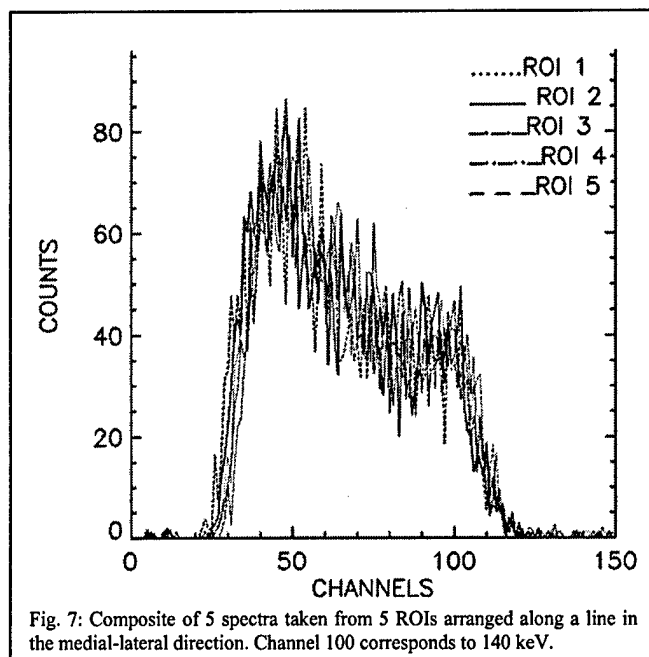


Fig. 7: Composite of 5 spectra taken from 5 ROIs arranged along a line in the medial-lateral direction. Channel 100 corresponds to 140 keV.

decreases with increasing distance from the chest wall for all patients, there is a large variation among patients in the value of the scatter fraction at a given distance.

We also examined the change in scatter fraction within the breast going in the left-right (or medial-lateral) direction. We found that the scatter fraction was essentially constant. Fig. 7 illustrates the consistency of the shape of the emission energy spectrum along this direction in an example image. The figure shows a composite of 5 spectra taken from 5 ROIs arranged along a line in the medial-lateral direction. They are virtually indistinguishable. We found that this was true for each of the breast images we tested, unless there was an abnormality present, such as a lesion with high radiotracer uptake.

We evaluated the dependence of the Compton scatter on breast thickness. Figs. 8 and 9 show the scatter fraction versus compressed breast thickness, for the left and right breasts, respectively. The scatter fractions shown were measured in a 1 cm x 1 cm (3 x 3 pixel) ROI centered 3.5 cm from the patient's chest wall. Each plot shows a trend towards increasing scatter with increasing breast thickness, however there is one case (compressed thickness of 5.5 cm for both breasts) in which exceptionally high scatter fractions were obtained. The reason for this outlier is unknown at present.

Fig. 10 shows an example of the result of scatter correction. The figure contains two profiles, each consisting of the same row of pixels, running in the chest to anterior direction. One profile is the uncorrected profile from the original scintigram, and the other is the same profile, but after removal of scatter counts. As can be predicted from Figs. 5 and 6, the number of scatter counts subtracted increases with decreasing distance from the chest wall. The region of uniform breast thickness (where the breast is in contact with the compression paddle) corresponds to the range from approximately 2 – 8 cm from the chest wall. The pixel count in this region is noticeably more constant following scatter

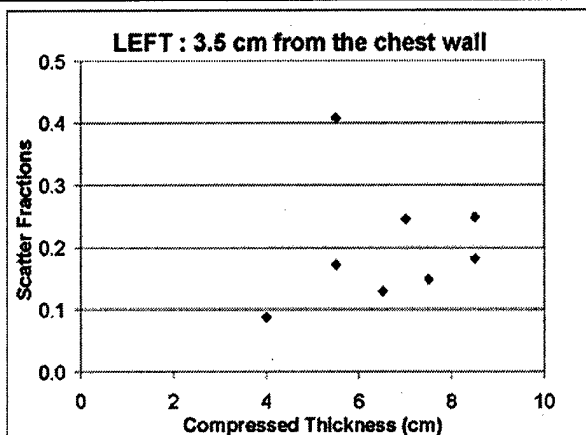


Fig. 8: Scatter fraction versus compressed breast thickness 3.5 cm from the chest wall, left breast.

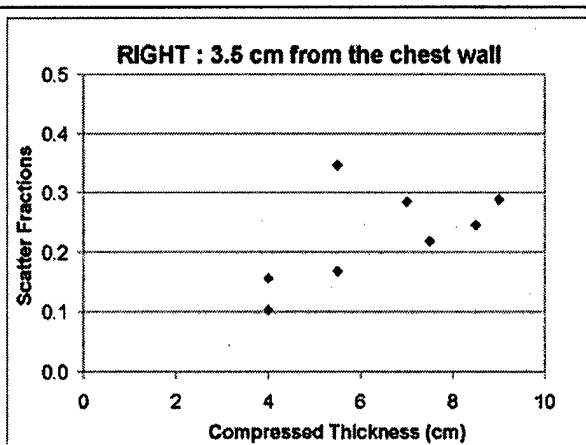


Fig. 9: Scatter fraction versus compressed breast thickness 3.5 cm from the chest wall, right breast.

correction, as would be expected if the counts were mainly primary counts arising from a volume of uniform thickness and concentration.

#### IV. DISCUSSION AND CONCLUSIONS

Although we have a limited number of cases thus far, several conclusions can already be made. In all cases studied, there is a marked decrease in Compton scatter with increasing distance from the chest wall. However, the value of the scatter fraction at a given distance from the chest wall varies substantially between patients (see Figs. 5 and 6). This variation indicates that 'universal' scatter corrections based simply on distance from the chest wall are not likely to work. Even after correction for variation in breast size, by examining scatter fraction at a given fraction of the chest wall-nipple distance, we found a similarly large inter-patient variation.

Although the amount of scatter radiation varies strongly in the chest-anterior direction, we found very little variation in the medial-lateral direction. In addition, the scatter fractions at a given location in the left and right breasts of any one patient are quite similar. This invariance was somewhat unexpected, given the strong uptake of sestamibi by the myocardium.

We also examined our dual modality images to determine whether there was any correlation between radiographic

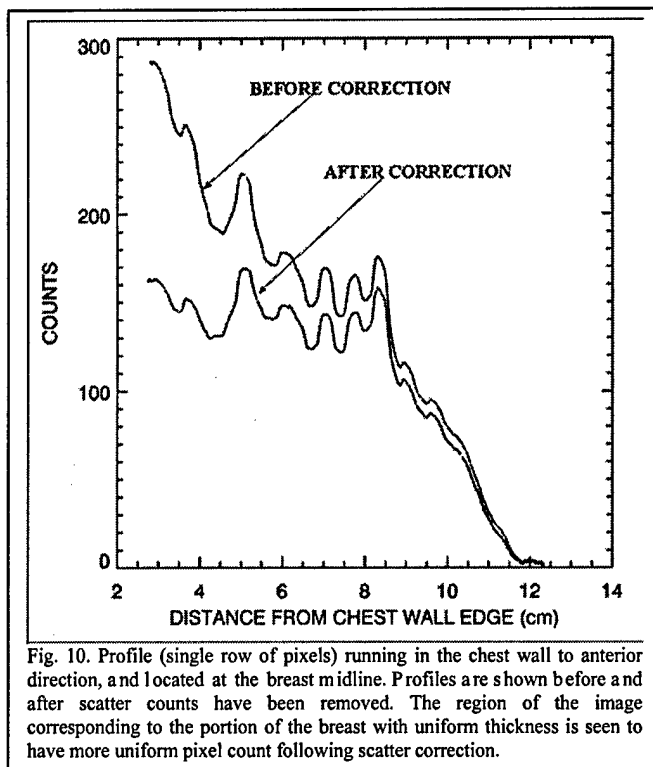


Fig. 10. Profile (single row of pixels) running in the chest wall to anterior direction, and located at the breast midline. Profiles are shown before and after scatter counts have been removed. The region of the image corresponding to the portion of the breast with uniform thickness is seen to have more uniform pixel count following scatter correction.

(mammographic) density and the scatter fraction. No apparent dependence on radiographic density was observed.

In general, the scatter fraction at a given distance from the chest wall increases with increasing breast thickness. However, the results shown in Figs. 8 and 9 do not take into account variation among patients in radiotracer concentration in the various parts of the body. The ratio of breast uptake to myocardial uptake, for example, could have a significant impact on the measured scatter fraction. While we have no way of measuring uptake in the heart and liver, an estimate can be made of the average radioactivity concentration in the breast in the region in contact with the compression paddle. Using the known gamma camera detection efficiency ( $\sim 10^{-4}$ ), the measured compressed thickness, and assuming an attenuation for breast tissue approximately equal to that of water ( $\mu \sim 0.155 \text{ cm}^{-1}$ ), we calculated the mean breast radioactivity concentration at the center of ROI 2. The mean value obtained from 12 images, 6 patient studies, is  $0.2041 \mu\text{Ci}/\text{cm}^3$ , with an inter-patient standard deviation of  $0.0672 \mu\text{Ci}/\text{cm}^3$ . This fairly large (33% of the mean) RMS variation among patients in concentration could partially explain the large variation we observe in scatter fraction at any given distance from the chest wall.

Position-dependent removal of scatter counts via estimation of the scatter fraction has the anticipated effect of making the pixel count in the uniform thickness region of a normal breast more uniform. However, even after removal of scatter counts, we observe that the total pixel count still increases slightly in the region near the chest wall. This could be the result of incomplete scatter removal, or may simply be indicative of a typical pattern of variation in radiotracer concentration

because of normal breast physiology (e.g. greater vascular density near the chest wall, or the proximity of muscle).

#### V. REFERENCES

- [1] M.B.Williams, M.More, D.Narayanan, A.G.Weisenberger, R.Wojcik, M.Stanton, W.Phillips, and A.Stewart, " Combined structural and functional Imaging of the breast " *Technology in Cancer Research and Treatment*, vol. 1, no. 1, pp. 39-42, February 2002.
- [2] R.Pani, F.Scopinaro, R.Pellegrini, A.Soluri, I.N.Weinberg, and G.De Vincentis, " The role of Compton background and breast compression on cancer detection in scintimammography " *Anticancer Research*, vol. 17, pp. 1645-1650, 1997.
- [3] F.J.T.Wackers, D.S.Berman, J.Maddahi, D.D.Watson, G.A.Beller, H.W.B.C.A.Stauss, M.Picard, B.L.Holman, R.Fridrich, E.Inglese, B.Deslaloys, A.Bischof-Delaloye, and L.M.K.Camin, " Technetium-99m hexakis 2-methoxyisobutyl isonitrile: Human biodistribution, dosimetry, safety, and preliminary comparison to thallium-201 for myocardial perfusion imaging " *J.Nucl.Med.*, vol. 30, pp. 301-311, 1989.

ORGAN	VOLUME (ml)	CONCENTRATION ( $\mu\text{Ci}/\text{ml}$ )
Heart (walls)	295	1.0
Liver	1015	3.9
Lung (right)	1162	0.51
Lung(left)	882	0.51
Torso	6500	0.33
Breast (right)	566	0
Breast (left)	566	0

Table 1: Concentrations of radioactivity used in the anthropomorphic phantom to obtain scatter-only breast emission spectra.

# X-ray Stereotactic Lesion Localization in Conjunction with Dedicated Scintimammography

Mitali J. Moré, Deepa Narayanan, Patricia J. Goodale, Stan Majewski, Benjamin Welch, Randolph Wojcik and Mark B. Williams, *Member, IEEE*

**Abstract**— We are developing a dual modality system that combines digital x-ray mammography with gamma emission scintigraphy on an upright mammography gantry. The breast is held under mild compression by a support structure that is independent of the detectors. The x-ray source and detectors can be rotated around a fixed rotation axis permitting multiple views of the breast with fixed compression. Two such views can be combined as a stereotactic pair to obtain the three-dimensional location of breast lesions. Information about the location of the lesion within the breast permits corrections for attenuation and detector spatial resolution, resulting in more accurate estimation of the true lesion-to-background concentration ratio, based on the image lesion-to-background counts ratio. In this paper, we describe the model used to make these corrections, and present the results of the phantom experiments designed to test the accuracy of our calculations.

**Index Terms**— breast imaging, technetium-99m sestamibi uptake, multimodality, scintimammography, stereotactic localization

## I. INTRODUCTION

Accurate preoperative staging of breast cancer is required to plan surgery and postoperative therapy. Scopinaro et al. have suggested that the uptake of technetium-99m sestamibi is correlated with angiogenesis and thus can be a potential marker for breast cancer invasiveness [1]. Other researchers have examined the degree of correlation between sestamibi uptake and the traditional indicators of malignancy such as desmoplasia and mitotic activity [2]. All these studies require quantification of the differential radiotracer uptake between the lesion and the surrounding healthy breast tissue. Since the depth of the lesion plays an important role in determining the contrast of the lesion in the image [3], it must be taken into account if accurate uptake values are to be obtained. The attenuation due to the structure overlying the

Manuscript received November 20, 2002. This work was supported in part by grants from the National Institutes of Health (grants RO1 CA69452 and RO1 CA66232), the US Army Breast Cancer Research Program (grant BC980469) and the Susan G. Komen Foundation (grant 99-003050).

M. J. Moré, M. B. Williams, P. J. Goodale and D. Narayanan are with the University of Virginia, Charlottesville, VA 22908 USA (telephone: 434-243-2687, e-mail: mjm4j@virginia.edu).

S. Majewski, B. Welch and R. Wojcik are with the Thomas Jefferson National Accelerator Facility, Newport News, VA 23606 USA. The Southeastern Universities Research Association (SURA) operates the Jefferson Lab for the United States Department of Energy under contract DE-AC05-84ER40150.

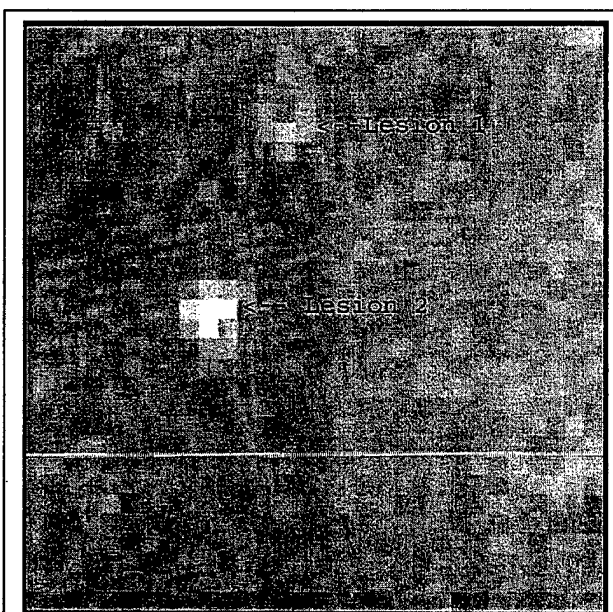


Fig. 1. Image showing 2 lesions of equal size and equal radioactivity concentration but placed at varying depth from the detector surface. The image contrast for lesion 1 is 0.26 and lesion 2 is 0.42. The true concentration ratio between the lesions and the background was 10:1.

lesion (between the lesion and the camera), and the detector blur, both act to reduce the lesion contrast in the image.

To illustrate the effects of attenuation and detector blur, an image of a phantom containing 2 simulated lesions is shown in Fig. 1. The image shows 2 lesions of equal size (inner diameter = 1 cm) and equal radioactivity concentration (3  $\mu\text{Ci/cc}$ ) but at different depths in the phantom, and therefore different distances from the detector. The background radioactivity concentration was 0.3  $\mu\text{Ci/cc}$ . Lesion 1 is at a distance of 7.7 cm from the detector whereas lesion 2 is at a distance of 5 cm. Even though the lesions have equal size and radioactivity concentration, their image contrast is vastly different. The image contrast for lesion 1 is 0.26 whereas that for lesion 2 is 0.42. This illustrates the fact that in order to quantify the radiotracer concentration, it is necessary to make corrections to the lesion-to-background contrast observed in the image.

We are developing a dual modality breast scanner with a digital x-ray detector and a gamma ray detector mounted on a single upright mammography unit. In the first generation of the scanner, the surface of the x-ray detector acts as the breast support [4]. Mild compression is applied and an x-ray and a



gamma image are obtained. Merging the two images together provides structural and functional information in a single image. The second generation dual modality breast scanner is designed to permit multiple views of the breast with fixed compression. The breast is held under mild compression on a breast support structure that is independent of the detectors and the gantry arm [5]. The x-ray source and the x-ray and gamma detectors are mounted on a motor-driven gantry arm. The motorized gantry with the breast support structure and a small field of view x-ray detector mounted on it is shown in Fig. 2. The mechanical aspects of this system have been described earlier [5]. Multiple view imaging makes it possible to obtain three-dimensional lesion localization with this

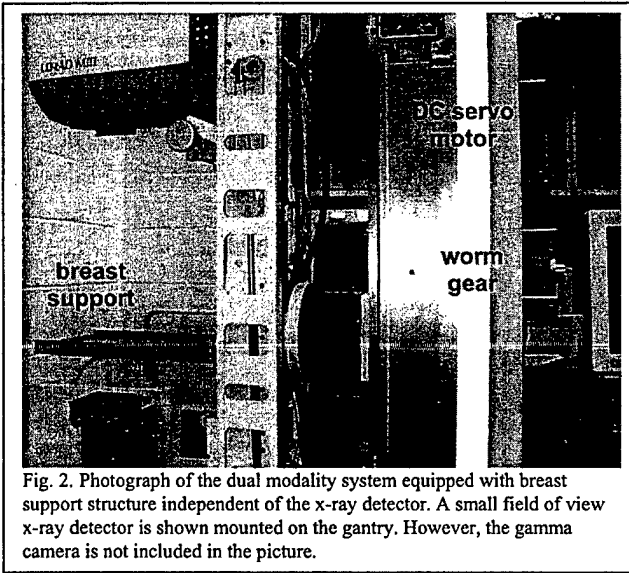


Fig. 2. Photograph of the dual modality system equipped with breast support structure independent of the x-ray detector. A small field of view x-ray detector is shown mounted on the gantry. However, the gamma camera is not included in the picture.

system.

## II. STEREOTACTIC LOCALIZATION

Lesion localization via stereotactic imaging is a method commonly used in breast needle biopsies [6-8]. The location of the lesion in the two stereo images is used to calculate the three-dimensional location of the lesion center,  $x_o$ ,  $y_o$ ,  $z_o$ . The expressions for  $x_o$ ,  $y_o$ ,  $z_o$  are given in (1)-(3), shown at the bottom of the page.

$$x_o = \frac{(a-c)\sin\theta((z_1x_2 + z_2x_1) + (a-c)(\sin\theta(z_1 - z_2) - \cos\theta(x_1 + x_2)))}{(z_1x_2 - z_2x_1) + (a-c)(\sin\theta(z_1 + z_2) + \cos\theta(x_1 - x_2)) - 2(a-c)^2\sin\theta\cos\theta} \quad (1)$$

$$z_o = \frac{x_o z_1 - (a-c)x_o \cos\theta - (a-c)z_1 \sin\theta + (a-c)x_1 \cos\theta}{x_1 - (a-c)\sin\theta} \quad (2)$$

$$y_o = \frac{L_{y1}(x_o - (a-c)\sin\theta)}{L_{x1}\cos\theta + x_{d1} - (a-c)\sin\theta} \quad (3)$$

The derivation of these equations and definition of the coordinate system and variables used are included in the appendix.

## III. THEORY

### A. Background Concentration

In the gamma emission image of the breast obtained in a dual modality scan, the average number of primary counts (i.e. not including scatter) per pixel ( $N_b$ ) in the background region of the image (i.e. a region of the breast adjacent to the lesion) can be calculated by integrating the activity along the thickness of the breast.

$$N_b = \epsilon t p^2 \int_0^D C_b(z) e^{-\mu_t z} dz \quad (4)$$

where  $\epsilon$  is the detection efficiency,  $t$  is the acquisition time,  $p$  is the pixel size, and  $C_b(z)$  is the activity per unit volume in the background portion of the breast.  $D$  is the thickness of the breast above the pixel and  $\mu_t$  is the linear attenuation coefficient of the breast tissue for 140 keV gamma rays. Since mild breast compression is used,  $D$  is simply the compressed breast thickness. In the case where the background activity concentration is uniform along the line of integration, this equation can easily be rearranged to calculate the background concentration.

$$C_b = \frac{N_b \mu_t}{\epsilon t p^2 [1 - e^{-\mu_t D}]} \quad (5)$$

The average number of counts obtained in a background pixel of the image is the sum of the scatter and the primary counts,  $N_b$ . These scatter counts must be subtracted from the sum to obtain the primary background counts. The scatter-to-primary ratio (SPR) is dependent on the location within the breast, increasing with decreasing distance from the chest wall [9]. In practice, the position-dependent SPR is obtained by acquiring images in list mode. This permits retrospective computation of position-dependent pulse height spectra from which the SPR can be obtained.

### B. Lesion Concentration

There are two primary factors that make the contrast of the lesion in the image a poor measure of the relative radiotracer concentrations in the lesion and the background breast tissue. These are i) the attenuation of gamma rays originating in the lesion, caused by the tissue overlying the lesion and ii) the blur due to the detector point spread function (PSF). In addition, for both lesion pixels and background pixels, scatter adds additional counts thus reducing the apparent concentration ratio in the image.

The lesion concentration is given by:

$$C_L = \frac{N_{L, total}}{V_L t \epsilon A} \quad (6)$$

where  $N_{L, total}$  is the total number of detected counts from the lesion,  $V_L$  is the lesion volume,  $t$  is the acquisition time,  $\epsilon$  is the gamma camera efficiency and  $A$  is the attenuation of the breast tissue overlying the lesion. The amount of attenuation is given by:

$$A = e^{-\mu_t b} \quad (7)$$

where  $b$  is the depth of the lesion in the breast.

The blurring due to the detector PSF does not change the total number of counts detected from the lesion but only redistributes these counts over a larger area thereby reducing the amplitude of the lesion peak in the image. The projection of the spherical lesion on a perfect detector (that is a detector whose PSF is a delta function) can be expressed as

$$N_L(x, y) = N_{L, \max} \left\{ 1 - \left[ \frac{|x - x_o|^2 + |y - y_o|^2}{R^2} \right] \right\}^{\frac{1}{2}} \text{ for } \frac{|x - x_o|^2 + |y - y_o|^2}{R^2} \leq 1$$

$$= 0 \text{ for } \frac{|x - x_o|^2 + |y - y_o|^2}{R^2} \geq 1 \quad (8)$$

where  $R$  is the lesion radius,  $x_o$  and  $y_o$  are the  $x$  and  $y$  co-ordinates of the lesion center and the peak amplitude  $N_{L, \max}$  is set by the condition:

$$\iint N_L(x, y) dx dy = N_{L, \text{total}} \quad (9)$$

To calculate the reduction in the amplitude at the lesion center in the image due to the PSF of the detector, the two-dimensional projection of the spherical lesion on the detector given by (8) is convoluted with the two-dimensional Gaussian PSF of the detector. The width of the Gaussian in both dimensions is a function of the distance of the source from the detector surface. The detector PSF, normalized for peak amplitude of unity, can be written as

$$g(x, y) = \exp \left( -\frac{(x - x_o)^2}{2\sigma_x^2} - \frac{(y - y_o)^2}{2\sigma_y^2} \right) \quad (10)$$

$$N_{L, \text{blur}}(x, y) = N_L(x, y) \otimes g(x, y) \quad (11)$$

Convolving the above two functions, we get the blurred spatial distribution of the detected lesion counts in the image,  $N_{L, \text{blur}}(x, y)$ . Clearly,  $N_{L, \text{blur}}(x, y)$  is spread over a larger area and has a reduced height relative to the original lesion projection,  $N_L(x, y)$ . The ratio of the peak amplitude of  $N_{L, \text{blur}}(x, y)$  to that of  $N_L(x, y)$  is defined as the contrast reduction coefficient (CRC) [3].

$$\text{CRC} = \frac{N_{L, \text{blur}, \max}}{N_{L, \max}} \quad (12)$$

The detector blur correction is applied by dividing the amplitude of the lesion profile in the image,  $N_{L, \text{blur}, \max}$  by the CRC.

$$N_{L, \max} = \frac{N_{L, \text{blur}, \max}}{\text{CRC}} \quad (13)$$

We thus obtain the amplitude of the lesion profile in the absence of detector blur,  $N_{L, \max}$  and can calculate the total number of detected lesion counts,  $N_{L, \text{total}}$  from (8) and (9) and finally the lesion concentration,  $C_L$  from (6).

#### IV. PHANTOM MEASUREMENTS

##### A. Lesion Localization with x-ray

A fillable phantom of rectangular cross section was designed to simulate a compressed breast. A tube was located at the phantom center to which spherical lesions were attached using low attenuation rods of known length,  $r$ , oriented at a known angle,  $\phi$  with respect to the phantom surface. A support was designed to allow the phantom to be mounted with the tube on the rotation axis of the gantry. A bearing allowed the gantry arm to rotate while the phantom was held stationary. This setup enabled us to place the lesions at accurately known  $x$ ,  $y$  and  $z$  co-ordinates. Lesions of interior diameter 0.8 and 1.0 cm from Data Spectrum Corp., Chapel Hill, NC were used for this study. The wall thickness of the lesions was only  $\sim 1$  mm and hence the attenuation through the walls could be ignored for the concentration calculation. With the phantom positioned independently of the x-ray detector, images were acquired at several different angles from  $-90$  to  $+90$  degrees. The phantom was filled with water and the lesions contained a small amount of gadolinium-DTPA for enhanced x-ray contrast.

##### B. Concentration Ratio Measurement

For simplicity, acquisition of the gamma images of the phantom was performed with the gamma camera positioned stationary on a bench top. A schematic of the experimental setup is shown in Fig. 3. The lesions and background were filled with a solution of technetium-99m with a lesion-to-background concentration ratio of 10:1 to simulate hot lesions in a warm background. The absolute concentration in the background was  $0.48 \mu\text{Ci/cc}$  and that in the lesion was  $4.9 \mu\text{Ci/cc}$ . In order to test our ability to measure concentration ratios over a range of lesion depths, the central tube of the phantom was attached to a rotation stage from Velmex, Inc.,

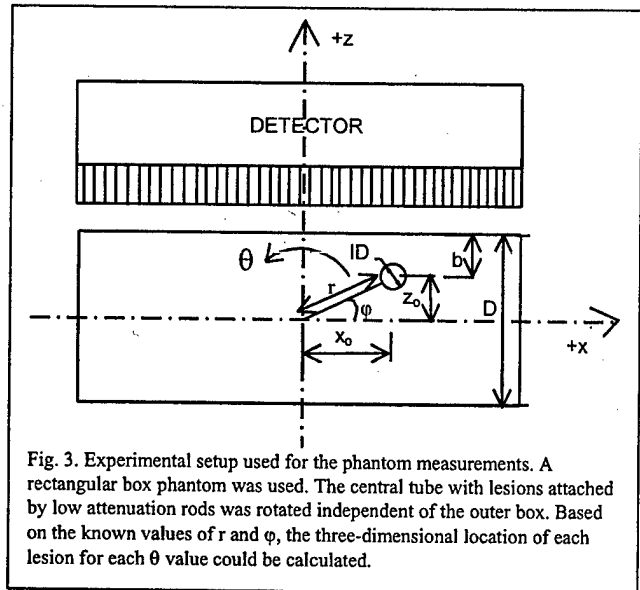


Fig. 3. Experimental setup used for the phantom measurements. A rectangular box phantom was used. The central tube with lesions attached by low attenuation rods was rotated independent of the outer box. Based on the known values of  $r$  and  $\phi$ , the three-dimensional location of each lesion for each  $\theta$  value could be calculated.

Bloomfield, NY (website: <http://www.velmex.com>), and rotated independently of the fixed phantom housing over a range of 360 degrees. At each angle,  $\theta$ , the co-ordinates  $x_0$ ,  $y_0$ ,  $z_0$  of the lesion centers were known based on the known rod lengths and angular spacing between lesions. Images were acquired every 15 degrees over a range of 360 degrees. Rotating the tube with respect to the phantom housing and detector surface places the lesions at varying depth and lesion-to-collimator distance, thereby permitting the correction model to be tested over a range of lesion depths with a single setup.

## V. DETECTOR CHARACTERIZATION

The gamma camera used for the studies described here consists of a 4 x 4 array of R7600-00-C8 position sensitive photomultiplier tubes (PSPMTs) from Hamamatsu, Bridgewater, New Jersey. The PSPMTs are optically coupled via acrylic light guides to a 30 x 30 array of NaI(Tl) crystals from Saint-Gobain, Newbury, Ohio. Each crystal is 3 mm x 3 mm x 6 mm (thick), and the crystal center-to-center spacing is 3.3 mm. The active field of view of the gamma camera is ~ 10 cm x 10 cm and the energy resolution is 15% at 140 keV. A lead collimator with 1.58 mm hexagonal apertures and height of 21 mm was used. The septal thickness was 0.267 mm. An energy window of -7%/+22% centered around the 140 keV photopeak was used. The camera sensitivity with this energy window is 220 cpm/ $\mu$ Ci (efficiency of  $1.0 \times 10^{-4}$ ). Further details on the detector design and performance are published elsewhere [10].

The full width at half maximum (FWHM) of the two-dimensional gamma camera PSF was obtained by measuring the image of a  $^{57}\text{Co}$  spot marker from Isotope Products, Valencia, CA at a variety of source-to-collimator distances. For each source-to-collimator distance, the spot marker, which has an active diameter of ~1.5 mm, was imaged at several locations on the detector surface. These images were shifted and summed to obtain a source image profile averaged over the camera surface. The profile of the point source,

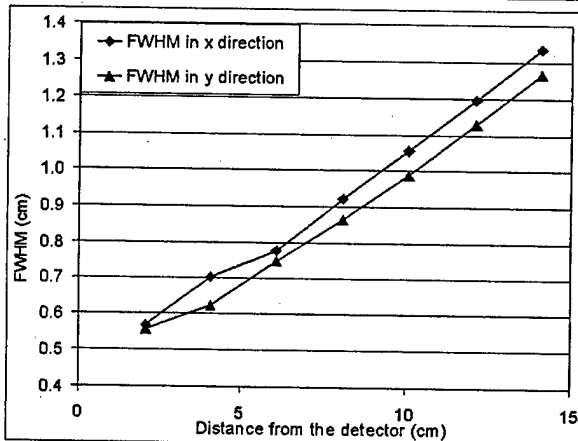


Fig. 4. Plot of the FWHM of the detector measured in two dimensions versus the distance from the detector.

which was assumed to be a uniform disc of diameter 1.5 mm, was deconvoluted from the averaged profile. The result was then fitted with a two-dimensional Gaussian function. The FWHM of the fitted function in the x- and y-dimensions are plotted as a function of the source to detector (source to crystal) distance in Fig. 4.

## VI. DATA ANALYSIS

### A. Lesion Localization

An analysis program written in IDL (Interactive Data Language from Research Systems, Inc., Boulder, CO, <http://www.rsinc.com>) was used to locate the lesion center in the stereo images. Using (1), (2) and (3) the co-ordinates of the lesion center were calculated. The z value of the lesion was then used to calculate the lesion and background concentration from the image counts.

### B. Concentration Ratio Measurement

1) *Background Concentration*: To get the number of background counts, a profile through the gamma image is taken which does not contain any lesions. For each lesion, profiles are extracted from rows near that lesion. From these rows, the average number of background counts is obtained using pixels taken from columns containing the lesion.

The scatter contribution to this background pixel count is subtracted to obtain the primary counts in the background. For the phantom used here, the scatter fraction is approximately constant and uniform throughout the region in which the lesions are located. The technique for obtaining the scatter fraction for a box phantom such as that used in these experiments has been described earlier [5]. The scatter fraction for the energy window -7%/+22% was measured to be 0.2. The background concentration is then determined from the primary background counts as described in (5).

2) *Lesion Concentration*: To calculate the lesion concentration, a region of interest centered on the lesion is first extracted. The number of counts in a pixel imaging the lesion is the sum of lesion counts and counts from the background volume above and below the lesion. The average number of background counts must be subtracted from the total number of lesion pixel counts to obtain the lesion-only counts. In order to obtain a good estimate of the amplitude of the lesion profile in the presence of statistical fluctuations, a two-dimensional surface is first fitted to the background subtracted lesion profile. This lesion profile amplitude must be divided by the CRC to compensate for the detector blur.

To obtain the CRC the following procedure is used. The known lesion-to-collimator distance is used to determine the x- and y-widths of the Gaussian detector PSF (Fig. 4). The PSF is convoluted with the theoretical lesion projection as in (11) and the theoretical CRC is obtained. The known lesion radius was used for the value of R in (8). The peak height obtained after dividing the fitted lesion amplitude by the CRC is then attributed to the maximum of the unblurred lesion projection function,  $N_L(x,y)$ , and the area under it is calculated to obtain the total counts coming from the lesion.

These counts are then divided by the attenuation of the overlying tissue. For the case of the phantom study reported here, the overlying tissue is water and the phantom wall. The attenuation of the gamma rays from the lesion is given by:

$$A = e^{-\mu_w b} A_{\text{wall}} \quad (14)$$

where  $\mu_w$  is the linear attenuation coefficient of water for 140 keV gamma rays and  $A_{\text{wall}}$  is the attenuation of the acrylic wall, on the camera side of the phantom.

## VII. RESULTS

### A. Lesion Localization

Table I shows the results obtained for the stereotactic localization using the x-ray imaging component of the dual modality system. These were obtained with stereo views at angles  $+15$  degrees and  $-15$  degrees. Columns 2 and 3 give the known location of the lesion center in the x and z dimensions and columns 4 and 5 give their location as calculated from the stereo views and equations. The last column gives the error, obtained by subtracting the calculated values from the known values in millimeters. Similar results were obtained using other stereo angles up to  $\pm 60^\circ$ .

TABLE I  
MEASURED AND CALCULATED LESION LOCATIONS

Lesion #	Known xo (cm)	zo (cm)	Calculated xo(cm)	zo(cm)	Difference x (mm)	z (mm)
1	-1.00	2.00	-0.99	2.04	-0.08	-0.39
2	4.00	1.00	4.02	0.96	-0.23	0.44
3	2.00	-1.00	2.00	-1.04	0.00	0.41
4	-3.00	0.00	-3.01	0.05	0.14	-0.48

### B. Concentration Ratio Measurement

Fig. 5 shows the ratios between the concentrations in two of the simulated lesions and the background, plotted as a function of the rotation angle of the central tube. Both lesions had an inner diameter of 1.0 cm and a lesion to background ratio of 10:1. Plots are shown of concentration ratios calculated both with and without corrections for detector blur, attenuation, and scatter. Corrected ratios were calculated using the method described above. Uncorrected concentration ratios were obtained for each view (all  $\theta$  values) as follows. ROIs were drawn containing the lesion image, and in a region nearby containing only background. The average background count per pixel was subtracted from each pixel in the lesion ROI. A smooth two-dimensional function was fitted to the resulting lesion profile, and its area was calculated. This area, divided by the known lesion volume, was taken as the lesion concentration. The background concentration was taken to be the total number of counts in the background ROI divided by the product of the ROI area and the phantom thickness. Fig. 5 shows that with corrections made, the concentration ratios are closer to the true concentration ratio.

Plot 6 shows, for every  $\theta$ , the image contrast obtained using the measured lesion and background pixel counts,

without any corrections made for attenuation or resolution degradation (squares). This illustrates that estimation of concentration ratios based simply on image contrast can be subject to large errors.

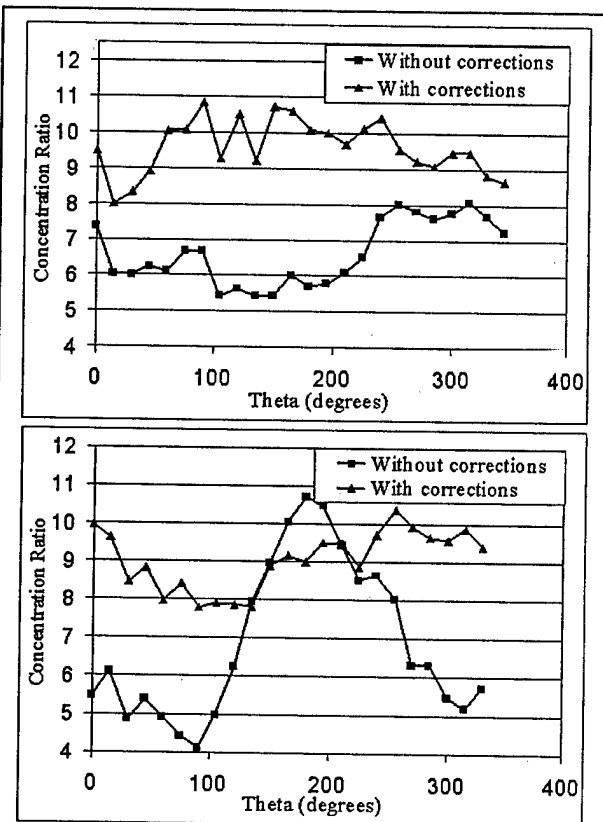


Fig. 5. Concentration ratios calculated with and without corrections plotted as a function of the rotation angle for two lesions with different  $r$  ( $r = 1.4$  cm in the upper graph and  $r = 2.7$  cm in the lower graph). The difference in the depth variation (2.8 cm versus 5.4 cm) is reflected in the difference in the shapes of the uncorrected curves.

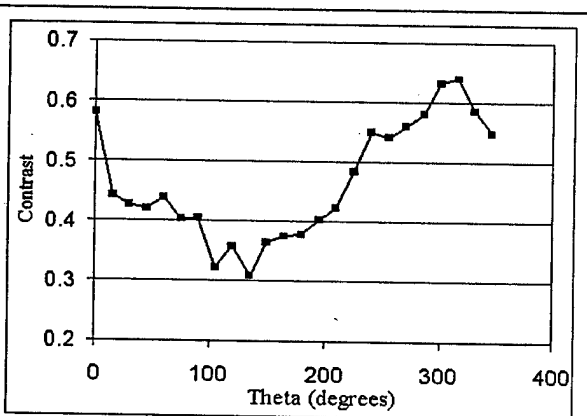


Fig. 6. Image contrast vs. rotation angle for the lesion whose concentration ratio is shown in the upper graph of Fig. 5.

## VIII. DISCUSSION AND CONCLUSIONS

The results obtained for the stereotactic lesion localization demonstrate accuracy to within 1-2 mm. This is accurate enough to be able to use the information to make corrections for the attenuation and detector blur and to significantly improve our estimate of the true concentration ratio in the tumor and the background, as is demonstrated in Fig. 5. However, for this phantom study, our calculations used the known lesion radius and volume. In the clinical situation, these parameters are unknown, and must be estimated from the images. Hence, methods need to be developed to extract this information from the high-resolution x-ray image. Similarly, the scatter fraction in the breast is a parameter that must be measured. The scatter fraction is a function of the location in the breast, and increases with decreasing distance to the chest wall [9]. Position-dependent energy spectra are routinely obtained during a dual modality scan, and can be used to obtain the position dependent scatter fraction.

In this paper we have described lesion localization using x-ray imaging. In principle, the three-dimensional lesion location could also be obtained using gamma ray stereo imaging [11]. However, gamma image acquisition times are significantly longer than those of x-ray images, and the accuracy of localization is lower due to the lower resolution of the gamma detectors. Also, it is desirable to have two x-ray views in order to better estimate the lesion shape and volume. We have therefore elected to use stereotactic x-ray imaging for lesion localization rather than gamma imaging. However, in situations where the lesion is poorly visualized radiographically (e.g. radiodense breasts), but is well visualized in the gamma images, stereotactic gamma localization would be the approach of choice.

Our phantom studies suggest that with appropriate corrections for attenuation, detector blur and scatter, based on measured lesion location, we can more accurately predict radioactivity concentration ratios. Stereotactic x-ray imaging combined with gamma ray imaging is a potentially powerful method to quantify radiotracer uptake in breast tumors.

## IX. APPENDIX

Following is the derivation of equations (1) - (3), which calculate the co-ordinates of the lesion center based on two stereo views. The co-ordinate system is shown in Fig. 7. We define the origin of the co-ordinate system to be the point on the rotation axis that is intersected by the line between the x-ray focal spot and the center point of the chest wall edge of the x-ray detector. The x-axis is defined to lie along the medial-to-lateral direction of the patient, with positive x pointing towards the right of the patient. The y-axis is along the rotation axis of the gantry with the positive direction going towards the gantry and away from the patient. The z-axis is defined to be along the detector to source direction when the gantry arm is positioned vertically, with positive z going towards the source. Let  $a$  be the source to detector distance and  $c$  be the distance between the origin and the center point of the chest wall edge of the detector surface.

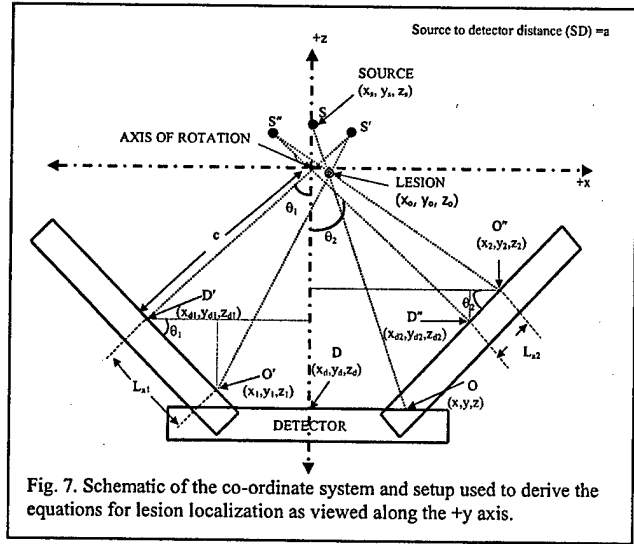


Fig. 7. Schematic of the co-ordinate system and setup used to derive the equations for lesion localization as viewed along the +y axis.

As shown in Fig. 7,  $(x_s, y_s, z_s)$  are the co-ordinates of the source,  $S$ , when the gantry arm is vertical ( $\theta = 0$ ) and  $(x_d, y_d, z_d)$  are the co-ordinates of the detector chest wall edge center,  $D$ , when  $\theta = 0$ .  $O(x, y, z)$  is the projection of the center of the lesion with spatial co-ordinates  $(x_o, y_o, z_o)$  on the detector plane.

If the source and detector are rotated through an angle  $\theta_1$ , the new source and detector center co-ordinates are  $S'(x_{s1}, y_{s1}, z_{s1})$  and  $D'(x_{d1}, y_{d1}, z_{d1})$  respectively, and the image of the lesion center on the detector is located at  $O'(x_1, y_1, z_1)$ . We denote the perpendicular distance in the images between the lesion center and the projection of the rotation axis onto the detector by  $L_{x1}$ , and denote the perpendicular distance between the lesion center and the chest wall edge of the detector by  $L_{y1}$ . From geometry we get the following relationships,

$$x_{s1} = (a - c) \sin \theta_1 ; \quad y_{s1} = 0 ; \quad z_{s1} = (a - c) \cos \theta_1$$

$$x_{d1} = -c \sin \theta_1 ; \quad y_{d1} = 0 ; \quad z_{d1} = -c \cos \theta_1$$

$$x_1 = L_{x1} \cos \theta_1 + x_{d1} ; \quad y_1 = L_{y1} ; \quad z_1 = z_{d1} - L_{x1} \sin \theta_1$$

The equation of line  $S'O'$  is given by,

$$\frac{x_o - x_{s1}}{x_1 - x_{s1}} = \frac{y_o - y_{s1}}{y_1 - y_{s1}} = \frac{z_o - z_{s1}}{z_1 - z_{s1}} \quad (15)$$

$$\frac{x_o - (a - c) \sin \theta_1}{x_1 - (a - c) \sin \theta_1} = \frac{z_o - (a - c) \cos \theta_1}{z_1 - (a - c) \cos \theta_1} \quad (16)$$

$$\text{Let } R = (a - c) \sin \theta_1$$

$$\text{and } T = (a - c) \cos \theta_1$$

then;

$$\frac{x_o - R}{x_1 - R} = \frac{z_o - T}{z_1 - T} \quad (17)$$

$$z_o = \frac{(x_o - R)(z_1 - T)}{x_1 - R} + T \quad (18)$$

For a negative rotation through an angle  $\theta_2$ , the new source and detector center co-ordinates are  $S''(x_{s2}, y_{s2}, z_{s2})$  and  $D''(x_{d2}, y_{d2}, z_{d2})$  respectively.  $O''(x_2, y_2, z_2)$  is the projection of the lesion center on the detector plane in this configuration. We now have the following equations,

$$\begin{aligned} x_{s2} &= (a-c)\sin\theta_2 ; y_{s2} = 0 ; z_{s2} = (a-c)\cos\theta_2 \\ x_{d2} &= -c\sin\theta_2 ; y_{d2} = 0 ; z_{d2} = -c\cos\theta_2 \\ x_2 &= L_{x2}\cos\theta_2 + x_{d2} ; y_2 = L_{y2} ; z_2 = z_{d2} - L_{x2}\sin\theta_2 \end{aligned}$$

The equation of line  $S''O''$  is given by,

$$\frac{x_o - x_{s2}}{x_2 - x_{s2}} = \frac{y_o - y_{s2}}{y_2 - y_{s2}} = \frac{z_o - z_{s2}}{z_2 - z_{s2}} \quad (19)$$

$$\frac{x_o - (a-c)\sin\theta_2}{x_2 - (a-c)\sin\theta_2} = \frac{z_o - (a-c)\cos\theta_2}{z_2 - (a-c)\cos\theta_2} \quad (20)$$

$$\text{Let } S = (a-c)\sin\theta_2$$

$$\text{and } U = (a-c)\cos\theta_2$$

$$\frac{x_o - S}{x_2 - S} = \frac{z_o - U}{z_2 - U} \quad (21)$$

$$z_o = \frac{(x_o - S)(z_2 - U)}{x_2 - S} + U \quad (22)$$

We can solve equations (18) and (22) simultaneously for  $x_o$  and  $z_o$ . We get;

$$x_o = \frac{R(z_1 - T)(x_2 - S) - S(z_2 - U)(x_1 - R) + (T - U)(x_1 - R)(x_2 - S)}{- (z_2 - U)(x_1 - R) + (z_1 - T)(x_2 - S)} \quad (23)$$

$$z_o = \frac{(x_o - R)(z_1 - T)}{(x_1 - R)} + T \quad (24)$$

If the two stereo views are chosen to be symmetric about the  $z$  axis then  $\theta_1 = -\theta_2 = \theta$  and

$$\cos\theta_1 = \cos\theta_2 = \cos\theta \quad \text{and} \quad \sin\theta_1 = -\sin\theta_2 = \sin\theta$$

We now substitute for  $R, S, T, U$  to get

$$x_o = \frac{(a-c)\sin\theta((z_1x_2 + z_2x_1) + (a-c)(\sin\theta(z_1 - z_2) - \cos\theta(x_1 + x_2)))}{(z_1x_2 - z_2x_1) + (a-c)(\sin\theta(z_1 + z_2) + \cos\theta(x_1 - x_2)) - 2(a-c)^2\sin\theta\cos\theta} \quad (25)$$

$$z_o = \frac{x_o z_1 - (a-c)x_o\cos\theta - (a-c)z_1\sin\theta + (a-c)x_1\cos\theta}{x_1 - (a-c)\sin\theta} \quad (26)$$

To solve for  $y_o$ :

$$\frac{x_o - x_{s1}}{x_1 - x_{s1}} = \frac{y_o - y_{s1}}{y_1 - y_{s1}} \quad (27)$$

$$\frac{x_o - (a-c)\sin\theta}{L_{x1}\cos\theta + x_{d1} - (a-c)\sin\theta} = \frac{y_o}{L_{y1}} \quad (28)$$

$$y_o = \frac{L_{y1}(x_o - (a-c)\sin\theta)}{L_{x1}\cos\theta + x_{d1} - (a-c)\sin\theta} \quad (29)$$

Equations (25), (26) and (29) are equations (1)-(3) in Section II.

## X. REFERENCES

- [1] F. Scopinaro, O. Schillaci, M. Scarpini, P. L. Mingazzini, L. Di Macio, M. Banci, R. Danieli, M. Zerilli, M. R. Limiti, A. Centi Colella, "Technetium-99m sestamibi: an indicator of breast cancer invasiveness", *European Journal of Nuclear Medicine*, vol. 21, no. 9, pp. 984-987, 1994.
- [2] John A. Cutrone, Lisa Shane Yospor, Iraj Khalkhali, Jorge Tolmos, Alessandro Devito, Linda Diggles, Maria Perla Vargas, Paul Shitabata and Samuel French, "Immunohistologic Assessment of Technetium-99m-MIBI uptake in benign and malignant breast lesions", *The Journal of Nuclear Medicine*, vol. 39, no. 3, pp. 449-453, 1998.
- [3] I. N. Weinberg, R. Pani, R. Pellegrini, F. Scopinaro, G. DeVincentis, A. Pergola and A. Soluri, "Small lesion Visualization in Scintimammography", *IEEE Transactions on Nuclear Science*, vol. 44, no. 3, pp. 1398-1402, June 1997.
- [4] M. B. Williams, M. J. More, D. Narayanan, S. Majewski, A. G. Weisenberger, R. Wojcik, M. Stanton, W. Phillips, A. Stewart, "Combined Structural and Functional Imaging of the breast", *Technology in Cancer Research and Treatment*, vol. 1, no. 1, pp. 39-42, February 2002.
- [5] Mark B. Williams, Mitali J. More, Deepa Narayanan, Stan Majewski, Ben Welch, and Douglas A. Kieper, "Phantom Study of Radiotracer Concentration Quantification in Breast Scintigraphy", *IEEE Transactions on Nuclear Science*, vol. 50 (3), pp. 433 - 438, June 2003.
- [6] Parker SH, Lovin JD, Jobe WE, Luethke JM, Hopper KD, Yakes WF, Burke BJ, "Stereotactic breast biopsy with a biopsy gun", *Radiology*, vol. 176, no. 3, pp. 741-747, September 1990.
- [7] L. Becker, D. Taves, L. McCurdy, G. Muscedere, S. Karlik and S. Ward, "Stereotactic core biopsy of breast microcalcifications: Comparison of film versus digital mammography, both using an add-on unit", *AJR. American Journal of Roentgenology*. 177(6): 1451-7, 2001 Dec.
- [8] H. M. Verkooijen, Core Biopsy After Radiological Localisation (COBRA) Study Group, "Diagnostic accuracy of stereotactic large-core needle biopsy for nonpalpable breast disease: results of a multicenter prospective study with 95% surgical confirmation", *International Journal of Cancer*, 99(6): 853-9, 2002 Jun 20.
- [9] Mark B. Williams, Deepa Narayanan, Mitali J. More, Patricia J. Goodale, Stan Majewski, Douglas Kieper, "Analysis of Position-Dependent Compton Scatter in Scintimammography With Mild Compression", *IEEE Nuclear Science Symposium Conference Record*, Norfolk, VA, Nov. 10-16, 2002.
- [10] S. Majewski, D. Kieper, E. Curran, C. Keppel, B. Kross, A. Palumbo, V. Popov, A. G. Weisenberger, B. Welch, R. Wojcik, M. B. Williams, A. R. Goode, M. More, G. Zhang, "Optimization of Dedicated Scintimammography Procedure using Detector Prototypes and Compressible Phantoms", *IEEE Trans. Nucl. Sci.* 48(3) 822-829 (2001).
- [11] I. Khalkhali, F.S. Mishkin, L.E. Diggles and S.R. Klein, "Radionuclide-guided stereotactic prebiopsy localization of nonpalpable breast lesions with normal mammograms", *Journal of Nuclear Medicine*, vol. 38, no. 7, pp. 1019-1022, 1997.